The neuronal calcium sensor Synaptotagmin-1 and SNARE proteins cooperate to dilate fusion pores mechanically

Zhenyong Wu[1,2], Nadiv Dharan[3], Sathish Thiyagarajan[3], Ben O'Shaughnessy[3,*], and Erdem Karatekin[1,2,4,5,*]

1 Department of Cellular and Molecular Physiology, Yale University, New Haven, CT

2 Nanobiology Institute, Yale University, West Haven, CT

3 Department of Chemical Engineering, Columbia University, New York, NY

4 Department of Molecular Biophysics and Biochemistry, Yale University, New Haven, CT

5 Centre National de la Recherche Scientifique, Paris, France

* Corresponding authors (bo8@columbia.edu and erdem.karatekin@yale.edu)

Lead contact: EK (erdem.karatekin@yale.edu)

ABSTRACT

All membrane fusion reactions proceed through an initial fusion pore, including calcium-triggered vesicular release of neurotransmitters and hormones. Expansion of this small pore to release cargo molecules is energetically costly and regulated by cells, but the mechanisms are poorly understood. Here we show that the neuronal/exocytic calcium sensor Synaptotagmin-1 (Syt1) promotes expansion of fusion pores induced by SNARE proteins, beyond its established role in coupling calcium influx to fusion pore opening. Fusion pore dilation by Syt1 required interactions with SNAREs, $PI(4,5)P_2$, and calcium. Calcium-induced insertion of the tandem C2 domain (C2AB) hydrophobic loops of Syt1 into the membrane is required for pore opening. We find that pore expansion also requires loop insertion, but through a distinct mechanism. Mathematical modelling suggests that membrane insertion re-orients the C2 domains bound to the SNARE complex, rotating the SNARE complex so as to exert force on the membranes in a mechanical lever action that increases the intermembrane distance. The increased membrane separation provokes pore dilation to offset a bending energy penalty. Our results show that Syt1 can assume a critical mechanical role in calcium-dependent fusion pore dilation during neurotransmitter and hormone release, distinct from its proposed role in generating curvature required for pore opening.

SIGNIFICANCE STATEMENT

Membrane fusion is a fundamental biological process, required for development, infection by enveloped viruses, fertilization, intracellular trafficking, and calcium-triggered release of neurotransmitters and hormones when cargo-laden vesicles fuse with the plasma membrane. All membrane fusion reactions proceed through a an initial, nanometer-sized fusion pore which can flicker open-closed multiple times before expanding or resealing. Pore expansion is required for efficient cargo release, but underlying mechanisms are poorly understood. Using a combination of single-pore measurements and quantitative modeling, we suggest that a complex between the neuronal calcium sensor Synaptotagmin-1 and the SNARE proteins together act as a calcium-sensitive mechanical lever to force the membranes apart and enlarge the pore, distinct from the curvature-generating mechanism of Synaptotagmin-1 proposed to promote pore opening.

Release of neurotransmitters and hormones occurs through exocytosis in which neurotransmitter-filled synaptic vesicles or hormone-laden secretory vesicles fuse with the plasma membrane to release their cargo to the extracellular space (1). The initial merger of the vesicular and plasma membranes results in a narrow fusion pore only ~1 nm in diameter (2-5). Dynamics of this key intermediate determine release kinetics and the mode of vesicle recycling. The fusion pore can fluctuate in size, flicker open-closed multiple times and either reseal after partial release of contents or dilate for full cargo release. Because many endocrine cells co-package small and large cargoes, the pore can additionally act as a molecular sieve, controlling the type of cargo released. In pancreatic β-cells, fusion pores that fail to dilate release only small cargo such as ATP, but not insulin, a process that occurs more commonly in type 2 diabetes (6). Adrenal chromaffin cells release small catecholamines through flickering small pores, or release additional, larger cargo, in an activity-dependent manner (7). Fusion pore dynamics also affect release of neurotransmitters and the mode of endocytosis during synaptic vesicle fusion (5, 8-14).

Little is known about the molecular mechanisms that control pore dilation. SNARE proteins, a core component of the release machinery, are known to influence fusion pore dynamics (15-23). Formation of complexes between the vesicular v-SNARE VAMP2/Syb2 and plasma membrane t-SNAREs Syntaxin-1/SNAP25 is required for fusion (24). Insertion of flexible linkers between the SNARE domain and the transmembrane domain in VAMP2, or truncation of the last nine residues of SNAP25, retard fusion pore expansion in adrenal chromaffin cells (20, 21, 25). Mutations in SNARE TMDs also affect fusion pores (18). Increasing the number of SNAREs at the fusion site accelerated fusion pore expansion in neurons (15, 26), astrocytes (27) and chromaffin cells (28) and led to larger pores in nanodisc-based single-pore fusion assays (15, 17). This was interpreted as due to increased molecular crowding at the waist of the pore with increasing SNARE copy numbers (17).

Synaptotagmins are another component of the release machinery known to affect fusion pore properties (29-39). They serve as the primary calcium sensors for exocytosis at most synapses and endocrine cells and couple membrane fusion driven by neuronal/exocytic SNAREs to calcium influx (40, 41). They are integral membrane proteins possessing two cytosolic C2 domains (C2A and C2B) which can bind Ca^{2+}, acidic lipids, SNAREs, and other effectors, but affinities vary widely among the 17 mammalian isoforms (41-48). Syt1 is the major neuronal isoform that mediates fast, synchronous neurotransmitter release (41, 45, 49). It resides in synaptic vesicles in neurons and secretory granules in neuroendocrine cells and interacts with SNAREs, acidic phospholipids, and calcium (1, 41, 50, 51). Calcium-binding to Syt1 causes hydrophobic residues at the tips of the Ca^{2+}-binding loops to insert into the membrane, generating curvature, which may be important for triggering fusion (37, 52, 53). In PC12 cells, membrane-insertion deficient mutants reduced exocytosis whereas mutants with enhanced insertion led to larger fusion pores (37), suggesting calcium-dependent curvature generation by Syt1 C2AB domains may also drive fusion pore expansion.

The mechanisms governing fusion pore expansion by Syt1 are not understood. Syt1-mediated membrane bending is thought to facilitate opening of the initial fusion pore by helping to bring the two membranes into close proximity, reducing the repulsive hydration forces by reducing the contact area, and exposing the hydrophobic interior of the two membranes to initiate lipid exchange (54, 55). Once the initial fusion pore is formed, however, it is not clear whether and how much curvature generation by Syt1contributes to fusion pore expansion. First, in PC12 cells multiple Syt isoforms reside on the same secretory granule and potentially compete for fusion activity (56, 57). Disrupting Syt1 function may allow another isoform to dominate fusion pore dynamics. In adrenal chromaffin cells where Syt1 and Syt7 are sorted to distinct granule populations, fusion pores of Syt7 granules dilate more slowly (38). Second, compared to Syt1 C2 domains, the higher calcium-affinity Syt7 C2 domains penetrate more avidly and deeply into membranes

(58, 59), which should lead to more efficient membrane bending (52, 53). This would appear to be inconsistent with the slower dilation of fusion pores by Syt7. Finally, previous reconstitutions could not probe the role of Syt1 in fusion pore regulation, as they lacked the required sensitivity and time resolution to detect single pores.

Here we investigated the mechanism by which Syt1 contributes to fusion pore dynamics, using a single-pore conductance assay (16, 17). Compared to SNAREs alone, addition of Syt1 increased the mean pore conductance three-fold. This effect required binding of Syt1 to calcium, SNAREs, and the acidic phospholipid $PI(4,5)P_2$. Thus, both pore opening and dilation are promoted by insertion of Syt1 C2AB top loops into the membrane in a Ca^{2+}-dependent manner, but we propose that distinct mechanisms are involved. Pore opening was previously suggested to be promoted by membrane curvature (52, 53). Here, mathematical modeling suggests that pore dilation relies on regulation of the intermembrane distance by Syt1. Syt1 penetration into the target membrane upon calcium binding re-orients the C2AB domains and SNARE complexes, forcing the membranes apart in a lever-like action that concomitantly expands the pore. Our results indicate a critical role for Syt1 in post-fusion pore dilation. The mechanism involves insertion of C2AB hydrophobic loops into the membrane, but is distinct from the well-established mechanism of C2AB-mediated curvature generation.

RESULTS

Co-reconstitution of Synaptotagmin-1 and v-SNAREs into nanolipoprotein particles

Previously, using a nanodisc-cell fusion assay, we characterized single, SNARE-induced fusion pores connecting a nanodisc and an engineered cell expressing neuronal "flipped" t-SNAREs ectopically (16, 17). In this assay, a flipped t-SNARE cell is voltage-clamped in the cell-attached configuration. Large nanodiscs called nanolipoprotein particles (NLPs, ~25 nm in diameter) (17, 60) reconstituted with the neuronal/exocytotic v-SNARE VAMP2 are included in the pipette solution. Fusion of an NLP with the cell surface creates a nanometer size pore that connects the cytosol to the exterior, allowing passage of ions under voltage clamp. Direct currents report pore size with sub-millisecond time resolution (16, 17).

To test whether Syt1 affected fusion pores in this system, we co-reconstituted ~4 copies of full-length Syt1 together with ~4 copies of VAMP2 (per disc face) into NLPs (vsNLPs, Fig. S1). We reasoned that, under these conditions potential modification of pore properties by Syt1 should be detectable. In the absence of Syt1, we previously found that only ~2 SNARE complexes are sufficient to open a small fusion pore (150-200 pS conductance), but dilation of the pore beyond ~1 nS conductance (~1.7 nm in radius, assuming the pore is a 15 nm long cylinder (61)) required the cooperative action of more than ~10 SNARE complexes (17). The increase in pore size was heterogeneous with increasing SNARE load; most pores remained small (mean conductance $\lesssim$ 1 nS), but an increasing fraction had much larger conductances of a few nS. With ~4 v-SNAREs per NLP face, fusion driven by SNAREs alone results in relatively small pores with ~200 pS average conductance, corresponding to a pore radius of ~0.76 nm (17). Larger pores (mean conductance>1 nS) are rare (<5%). With ~25 nm NLPs, a fusion pore can in principle grow to >10 nm diameter (~9 nS conductance) before the scaffold protein stabilizing the edges of the NLP becomes a limitation for further pore dilation (17). Thus, at this v-SNARE density, there is a large latitude in pore sizes that can be accommodated, if introduction of Syt1 were to lead to any modification.

We tuned NLP size by varying the lipid-to-scaffold protein (ApoE422k) ratio and adjusted copy numbers of VAMP2 and Syt1 until we obtained the target value of ~4 copies of each per NLP face, similar to

previous work with SNAREs alone (17, 60). vsNLPs were purified by size exclusion chromatography and characterized by SDS-PAGE and transmission electron microscopy (Fig. S1B-D). The distribution of NLP diameters was fairly narrow, with mean diameter 25 nm (±5.6 nm SD, Fig. S1E), and did not change significantly compared to the distribution when v-SNAREs alone were incorporated at ~4 copies per face (mean diameter = 25 ± 4 nm, (Fig. S1F-H, and (17)).

Syt1 promotes fusion pore expansion

To probe fusion pores, we voltage-clamped a flipped t-SNARE cell in the cell-attached configuration and included NLPs co-loaded with Syt1 and VAMP2 in the pipette solution as shown in Fig. 1 (100 nM vsNLPs, 120 μM lipid). In the absence (with 0.5 mM EGTA in the buffer) or presence of 100 μM free calcium pore properties were affected only slightly compared to the case when Syt1 was omitted from the NLPs (Figs. 1 and 2). Syt1 interacts with acidic lipids, in particular with $PI(4,5)P_2$, in both calcium dependent and independent manners, and these interactions are required for Syt1's ability to trigger membrane fusion (30, 62-66). However, the outer leaflet of the plasma membrane which is seen by Syt1 in our assay is poor in such lipids. We wondered whether the lack of acidic lipids in the outer leaflet of the cell membrane could be a limitation for Syt1's ability to modulate fusion pores. To test for this possibility, we incubated flipped t-SNARE cells with with 20 μM $diC_8PI(4,5)P_2$ for 20 min and rinsed excess exogenous lipid. At different time points after rinsing, we probed incorporation of the short-chain $PI(4,5)P_2$ into the outer leaflet of the cell membrane by immunofluorescence, using a mouse monoclonal anti-$PI(4,5)P_2$ primary antibody, without permeabilizing the cells (Fig 1B). The signal decreased slightly as a function of time but persisted for at least 80 min. To compare the level of short-chain $PI(4,5)P_2$ incorporated into the outer leaflet in this manner with endogenous $PI(4,5)P_2$ levels in the inner leaflet, we measured immunofluorescence from permeabilized cells that were not incubated with $diC_8PI(4,5)P_2$. Outer leaflet $diC_8PI(4,5)P_2$ levels were within 25% of the endogenous inner-leaflet $PI(4,5)P_2$ levels (Fig. 1B).

When we repeated vsNLP-flipped t-SNARE cell fusion experiments with cells pre-incubated with $diC_8PI(4,5)P_2$, the rate of fusion in the absence of calcium was unchanged compared to fusion with SNAREs alone, but increased 3-4 fold when 100 μM calcium was present (Fig. 2A). Compared to SNARE-alone fusion, the mean single-pore conductance increased only slightly in the absence of calcium but was three-fold larger in the presence of 100 μM calcium (Fig. 2B). Bursts of pore currents lasted longer in the presence of Syt1, calcium and $PI(4,5)P_2$, compared to conditions in which Syt1 or calcium were omitted (Fig. S2). Conductance fluctuations around the mean value were also larger when Syt1, calcium and $PI(4,5)P_2$ were all present (Fig. S2). For all cases tested, the number of pore flickers ($N_{flickers}$) and burst durations (T_o) were well-described by geometric and exponential distributions, respectively (Fig. S2), as would be expected for discrete transitions between open, transiently blocked, and closed states(67). Fusion was SNARE-dependent, as treatment with the tetanus neurotoxin TeNT, which cleaves VAMP2 at position 76Q-77F and blocks exocytosis (68), dramatically reduced the fusion rate of vsNLPs even in the presence of calcium and exogenous $PI(4,5)P_2$ (Fig 1D and Fig 2A). Thus, Syt1 increases the fusion rate and promotes pore dilation during SNARE-induced fusion, in a calcium and $PI(4,5)P_2$ dependent manner.

We pooled individual current bursts to obtain the distributions for fusion pore conductances and pore radii as shown in Fig. 2C, D, and Figure S3. The distributions were similar for SNAREs alone, whether calcium or $PI(4,5)P_2$ were added, and with Syt1 when calcium was omitted (Fig. 2C, D, and Fig. S3). By contrast, in the presence of 100 μM free calcium and exogenous $PI(4,5)P_2$, larger conductance values (and corresponding pore radii) became more likely (Fig. 2C,D).

Even when pores were maximally dilated by Syt1, the mean conductance and pore radius, $G_{po} = 595$ pS (S.E.M.$= 51$ pS), and $r_{po} = 1.13$ nm (S.E.M$= 0.04$ nm) were significantly less than the maximum possible value predicted from NLP dimensions (17). That is, the geometric constraints imposed by the NLP dimensions were not limiting pore expansion. Instead, there is inherent resistance to pore dilation, independent of NLP scaffolding (17) as predicted and observed in other systems (69-71). To quantify the resistance, we computed the apparent pore free energy $U(r_{po})$ from the distribution of pore radii, $P(r_{po}) \sim e^{U(r_{po})/kT}$ for fusion with both SNAREs alone and with Syt1 under optimal conditions (with exogenous PI(4,5)P_2 and 100 μM free calcium). With SNAREs alone, or with Syt1 but in the absence of calcium, the free energy profile suggested that ~6-7 kT energy was required to expand the pore from 1 to ~2.5 nm radius, whereas calcium-bound Syt1 reduced this resistance to ~2 kT (Fig. 2E). That is, the force opposing pore expansion decreased from 16-19 pN in the absence of calcium to ~5 pN in the presence of 100 μM calcium.

We tested if the soluble C2AB domains of Syt1 could recapitulate these results. We included 10 μM C2AB together with NLPs reconstituted with ~4 copies per face of VAMP2 in the patch pipette and monitored fusion with flipped t-SNARE cells in the cell attached configuration under voltage clamp. Similar to the results with full-length Syt1, there was little change in fusion rate and mean conductance compared to the SNARE-alone case, unless calcium and exogenous PI(4,5)P_2 were also present. In the presence of 100 μM calcium and short-chain PI(4,5)P_2, fusion rate and mean pore conductance were stimulated to the same degree as when full-length Syt1 was used (Fig. 2). The distributions of average single pore conductances (Fig. 2F), conductance fluctuations, pore lifetimes, and other pore parameters were indistinguishable whether full-length Syt1 or soluble C2AB were used (Figs. S2 and S3). The apparent free energy profile calculated from the pore size distribution was also indistinguishable from that of full-length Syt1 (Fig. 2E). We conclude that soluble Syt1 C2AB recapitulates the effect of full-length Syt1 on promoting SNARE-mediated fusion pores. As they were far easier to manipulate, we used soluble Syt1 C2AB domains for the remainder of this work.

Pore dilation by Synaptotagmin-1 C2AB requires binding to calcium, PI(4,5)P_2, and SNAREs

We further tested the requirement for Syt1 C2AB binding to calcium, PI(4,5)P_2, and SNAREs for promoting pore dilation, using mutagenesis (Fig. 3). Binding of calcium to the second C2 domain of Syt1 is known to be essential for evoked release(41, 72, 73). When calcium binding to the C2B domain was impaired by mutating a highly conserved aspartate to asparagine (Syt1 C2AB D309N(74)), mean single pore conductance returned to the value obtained in the presence of SNAREs alone (Fig. 3C). The rate at which current bursts appeared also returned to the SNARE-alone level (Fig. 3B). Other pore properties were also indistinguishable from the SNARE-alone case (Fig. S4). We conclude that calcium binding to Syt1 C2B is essential for fusion pore dilation, in addition to its well-known role for triggering the opening of a fusion pore.

The C2B domain of Syt1 possesses a polybasic patch (K324-327) that interacts with acidic phospholipids (Fig. 3A) and is important for synchronous evoked release (66). Although this interaction occurs in the absence of calcium(41), it contributes to the membrane binding energy of C2AB in the presence of calcium (62), presumably because multivalent interactions increase the bound lifetime of C2AB. Partially neutralizing the polybasic patch in C2B (K326A, K327A) reduced the fusion rate, and resulted in single pore conductances that were indistinguishable from those for SNARE-alone pores (Fig. 3). Similarly, the burst lifetime returned to the SNARE-alone level, but conductance fluctuations and the flicker rate were reduced, while there was a slight increase in the pore open probability, i.e. the fraction of time the pore

was open during a burst (Fig. S4). Thus, in addition to its established role in evoked release (66, 75), the polybasic patch in Syt1 C2B is also required for fusion pore dilation.

Two recent crystal structures identified a "primary" interaction interface between Syt1 C2B and the four-helical SNARE complex (76, 77) (Fig.3A). Specifically, two arginines (R398 and R399) form salt bridges with glutamates and aspartates in a groove between SNAP25 and Syntaxin-1 (76). Mutation of these arginines to glutamines (R398Q, R399Q) was shown to largely abolish evoked release from hippocampal neurons (66, 76, 78), likely by disrupting the interaction of Syt1 C2B with SNAREs (66, 76) (but see (78, 79)). When we used purified C2AB bearing the same mutations ($C2AB^{R398Q,\ R399Q}$) both the fusion rate and the mean pore conductance decreased significantly, close to SNARE-alone levels (Fig. 3B, C). Burst lifetimes and conductance fluctuations were not significantly different than for pores induced by SNAREs alone, but the flicker rate was lower and pore open probability was larger (Fig. S4).

Together, these results indicate that binding of Syt1 to calcium, $PI(4,5)P_2$, and SNAREs, which are all crucial for Syt1's role in evoked neurotransmitter release (1, 41), are also essential for its function in dilating SNARE-induced fusion pores.

Calcium-dependence of pore dilation by Syt1 C2AB

To determine whether pore properties are altered by calcium, we varied the free calcium concentration in the pipette solution and repeated the fusion experiments. Mean open-pore conductance $\langle G_{po} \rangle$ increased with increasing calcium (Fig. 4A), consistent with a mathematical model (see below). The pore open probability during a burst similarly increased as a function of calcium (Fig. 4B). Conductance fluctuations and burst lifetimes also increased, while the flicker rate decreased as $[Ca^{2+}]$ was increased (Fig. S5). That is, pores tended to spend more time in the open state with higher calcium, and the open state conductance increased.

The conductances in the open-state and the corresponding pore radii (r_{po}) were broadly distributed at all calcium concentrations tested, but the distributions did not shift uniformly as calcium increased (Fig. S5). The apparent free energy profiles, estimated from the pore size distributions, are plotted in Fig. 4C. With increasing calcium, the well around the most likely radius (~0.5-0.7 nm) became wider, and the slopes of the energy profiles for radii above the well's upper boundary, reflecting the force needed to dilate the pore, decreased as calcium increased. The calcium concentration at which this transition occurs (20-50 μM) is consistent with the known calcium binding affinity of Syt1(62, 63, 65, 80, 81).

Calcium-dependent membrane-insertion of Syt1 C2AB is necessary for pore dilation

Calcium binds simultaneously to acidic phospholipids and highly conserved aspartate residues in a pocket formed by loops at the top of the beta-sandwich structure of the Syt1 C2 domains(41, 73, 82). Hydrophobic residues at the tips of the loops flanking the calcium-binding residues in Syt1 C2A (M173 and F234) and C2B (V304 and I367) insert into the membrane as a result of these interactions, strengthening membrane binding of C2 domains(41, 62, 83). Membrane insertion of these hydrophobic residues expands the membrane in one leaflet, creating an area mismatch, which relaxes as the membrane curves away from the wedge-like insertion. This membrane buckling is thought to contribute to the triggering of release(37, 52, 53). We wondered whether membrane-insertion of hydrophobic loops played any role in pore dilation. To test this, we introduced mutations that made the loops insertion-deficient (M173A, F234A, V304A and I367A, the "4A" mutant (37, 52)) or that increased membrane affinity, leading to increased membrane curvature (M173W, F234W, V304W and I367W, the "4W" mutant (37, 52)).

In the nanodisc-cell fusion assay, the membrane penetration deficient 4A mutant was non-functional, having no discernible effect on pore dilation or the fusion rate (Fig. 5). By contrast, the 4W mutant which inserts into the membrane more avidly essentially behaved like the wild-type C2AB, with the exception that the pore dilation ability of the 4W mutant was less dependent on the presence of $PI(4,5)P_2$ (Fig 5C and Fig. S6).

The rates of fusion between liposomes (52, 53) and exocytosis (37, 84) correlate well with the curvature-generation ability of the Syt1 mutants. Here, we found that the 4W mutant with increased curvature-generation ability did not lead to larger pores compared to wild-type C2AB. We thus wondered whether membrane-penetration could dilate fusion pores using a distinct mechanism. To address this issue, we turned to mathematical modeling.

Mathematical modelling suggests that Syt1 and SNARE proteins cooperatively dilate fusion pores in a mechanical lever action

How do Syt1 and SNAREs cooperate to expand the pore in the presence of calcium? To help elucidate the mechanism, we developed a detailed mathematical model of the membrane fusion pore in the presence of SNARE proteins and the C2AB domain of Syt1 (see SI Appendix for model details and parameters). The energetics of the fusion pore membrane are described in the classic Helfrich framework, with contributions from bending energy and membrane tension, and for simplicity we assume the fusion pore belongs to a toroidal family of possible shapes (85-88). To compare directly with the present experiments, we incorporate 4 SNARE complexes, each of which can either be in the *trans* configuration and free to roam the fusion pore, or else fully zippered in the *cis* configuration near the waist, Figure 6A (17). The model accounts for the SNARE zippering energy which favors full zippering (89, 90), and for crowding interactions among zippered SNAREs which favor partial unzippering into the *trans* state, an entropic effect (17, 91).

Syt1 C2B domains are assumed bound to each SNARE complex at the so-called primary interface identified in recent crystal structures (76, 77) (Fig. 3A). When Ca^{2+} is bound to the C2AB domain loops, the loops may be buried or unburied in the membrane with a relative probability that depends on the calcium concentration according to the Hill equation (36, 80). We use a Hill coefficient of 2.3, and the measured affinity of calcium for Syt1 in the presence of $PI(4,5)P_2$-containing membranes (65). Without calcium, the loops are assumed unburied.

Thus, the model permits two configurations of the SNARE-C2AB complex, implemented according to the crystal structure (PDB ID 5ccg (76)), Figure 6B. **(1)** With bound Ca^{2+}, the C2AB complex can be in the buried state, in which the C2B polybasic patch lies ~ 0.5 nm from the membrane (92) and the C2A and C2B domains are anchored to the membrane by their calcium-binding loops, reported to penetrate ~1 nm deep (93). We find that these constraints imply that the C2B anchoring tilts the SNAREpin "upwards" at ~ 15° to the plasma membrane, pushing against the membranes and constraining the pore height to be no less than ~ 5.5 nm, Figure 6B. **(2)** With no bound calcium, the C2B polybasic patch (94) and the SNAREpin orient parallel to the plasma membrane, providing minimal constraint on the pore height (the maximum thickness of the SNARE-C2B cross-section is ~ 3 nm, less than the height due to entropic forces among SNAREpins, see below). This unanchored state is also accessible when calcium is bound, with a probability that decreases with increasing calcium concentration.

Given the microscopically long pore lifetimes of seconds, we assumed the fusion pore-SNARE-Syt1 system has sufficient time to equilibrate. For a given pore radius, r_{po}, we calculated the free energy by summing over all allowed SNARE-C2AB configurations, all pore heights consistent with the constraints

imposed by the SNARE-C2B complex, and all possible numbers of zippered SNAREs. Each state in this sum is weighted by its Boltzmann factor, yielding the free energy $U(r_{\mathrm{po}})$ and pore size distribution ~ $\exp[-U(r_{\mathrm{po}})/k_{\mathrm{B}}T]$ (SI Appendix).

The predicted free energy profiles with and without calcium are close to the experimental profiles, as shown in Figure 6C. We compared model and experimental free energies up to a maximum pore size of 4 nm, since sampling for larger pores was limited in the experiments. In agreement with experiment, introduction of calcium is predicted to increase the pore size fluctuations, as reflected by the broader distribution. From these pore size statistics, we calculated mean pore sizes and conductances. In the absence of calcium, the model predicts a mean fusion pore radius ~1 nm and a mean height ~ 4.5 nm, due to entropic crowding effects among *cis* SNARE complexes (17), Figure S7 and Table S2 . These crowding effects expand the pore relative to the SNARE-free case, since a bigger pore increases the entropy of *cis*-SNAREs at the waist by providing more space.

When Ca^{2+} is introduced at high saturating concentrations, the model predicts a ~ 1.6-fold increase of pore radius to ~1.7 nm, or a ~2.3-fold increase in conductance, close to the experimentally measured ~2.2-fold increase (Figure 6D and Table S2). The pore expansion mechanism is the upward tilt of the SNAREpin due to the anchoring by the C2B Ca^{2+} binding loops, forcing the pore height to exceed ~ 5.5 nm (we found a mean height of ~ 6.2 nm) (Figure 6B, E and Table S2). Downward force from the membranes was unable to swivel the SNAREpin due to the anchoring by the loops, whose removal from the membrane is highly energetically unfavorable(62).

Figure 6D shows the predicted dependence of normalized pore conductance on calcium concentration, compared with the experimental values. Consistent with experiment, the predicted values interpolate between the calcium-free and saturating calcium conductances, with a sharp upturn at ~ 20 μM.

In summary, our model suggests a mechanism in which the SNARE-C2AB complex is a calcium-triggered mechanical lever that enlarges the fusion pore in cooperation with entropic forces generated by SNARE complexes (Figure 6E). On addition of Ca^{2+}, the C2AB domain rotates and inserts its calcium binding loops into the membrane, tilting the SNARE complex so that it pushes the membrane surfaces further apart in a lever action. Since this increase in pore height would otherwise increase the net membrane bending energy, the pore diameter increases to offset this penalty (see SI Appendix). This creates more room for additional SNAREs to zipper into the pore waist and enhance the entropic forces that also promote pore expansion, enabling additional Syt1-SNARE complexes to contribute to pore expansion as mechanical levers. Thus, post fusion, Syt1 and SNAREs cooperatively mediate calcium-dependent regulation of fusion pore size by mechanical effects.

DISCUSSION

Membrane fusion occurs in stages. First, membranes are brought into close apposition to overcome repulsive hydration forces. Second, a small, nascent fusion pore forms, connecting the fusing membranes. Third, the initial small pore expands to allow passage of cargo molecules (2-4). Among different stages of membrane fusion, pore expansion can be energetically one of the costliest (69, 70, 95-97). Consistent with this notion, fusion pores connecting protein-free lipid bilayers fluctuate, flicker open-closed, and eventually reseal unless external energy is supplied in the form of membrane tension (98), while the initial fusion pore during biological membrane fusion is a metastable structure whose dynamics are regulated by cellular processes (3-7, 10, 71, 99-102).

Several mechanisms regulating fusion pore dynamics have recently emerged. First, membrane tension promotes fusion pore dilation during exocytosis, often through cytoskeleton-plasma membrane interactions (103-105). Second, neuronal/exocytic SNARE proteins promote fusion pore dilation by providing entropic forces due to molecular crowding at the pore's waist (17), consistent with the observation that increased SNARE availability results in larger, or faster expanding pores (15, 17, 26-28). Third, during yeast vacuole-vacuole fusion, increased fusogen volume has been suggested as a mechanism that stabilizes fusion pores (71, 106). However, these mechanisms cannot explain fusion pore dilation during exocytosis, because none are calcium-dependent, in contrast to exocytic fusion pore expansion (32, 107-109).

Here, we found that Syt1 has roles in both fusion pore formation and dilation, consistent with studies in secretory cells (32, 37). Syt1promotes expansion of SNARE-induced fusion pores in a calcium-, acidic lipid-, and SNARE-dependent manner. Modeling suggests the major contribution of Syt1 to pore dilation is through its mechanical modulation of the inter-membrane separation. A larger separation drives the pores to be larger to offset the increased bending energy that would be generated by the increased pore height, as predicted from membrane mechanics (17).

How can Syt1 modulate the intermembrane separation? Previous work showed calcium binding to isolated Syt1 C2 domains leads to insertion of the hydrophobic residues at the tips of the calcium-binding loops into the membrane (41, 93, 94). In the presence of $PI(4,5)P_2$, calcium-bound C2B assumes a conformation in which its long axis is tilted with respect to the membrane normal, as it interacts with the membrane simultaneously through its calcium binding loops and the polybasic patch (K324-327) bound to $PI(4,5)P_2$ (92). When present, C2B also binds the t-SNAREs Stx1 and SNAP25, with its long axis parallel to the SNARE bundle, in a calcium-independent manner (76). In this orientation, the polybasic patch on C2B (K324-327) is free to interact with acidic lipids on the target membrane (76). At low, resting amounts of calcium, the calcium-free SNARE-C2B complex is therefore expected to lie parallel to the membrane, with the C2B domain simultaneously interacting with target membrane acidic lipids and the SNARE complex (76) (Fig. 6). The SNARE-Syt complex in this parallel configuration is ~3 nm thick, only slightly larger than the SNARE bundle itself, and therefore does not increase the interbilayer separation appreciably compared to the case with SNAREs alone. By contrast, in the presence of high calcium, the calcium-bound C2B domain will tend to reorient such that its hydrophobic top loops insert into the target membrane, resulting in a tilting of the SNARE complex of ~15 degrees, which will push the membranes ~5-6 nm apart (Fig. 6). The increased intermembrane separation quantitatively accounts for the conductance increase in the presence of Syt1, and its requirements for intact calcium, and SNARE-binding regions on C2B.

Syt1 was previously proposed to regulate membrane apposition (66, 110-113), preventing fusion pore opening at low calcium by maintaining the membranes >5-8 nm apart, halting complete SNARE zippering. Upon calcium binding to Syt1, this distance is reduced to <5 nm (66), sufficient for SNAREs to complete their zippering and initiate fusion. During the pore opening stage, curvature generation by insertion of Syt1's hydrophobic loops into the membranes may contribute to pore opening (37, 52, 53), since buckling the membranes toward each other to form a nipple would reduce the energy barriers opposing membrane merger, by at least three mechanisms. First, nipple formation would bring the two membranes into close proximity. Second, dimpling would reduce the initial contact area, minimizing the repulsive hydration forces opposing fusion. Third, the nipples would facilitate exposure of hydrophobic defects facing the two membranes, allowing inter-membrane lipid exchange. In addition to opening the fusion pore, Syt1 also contributes to the dilation of the nascent fusion pore (32, 37), but the mechanisms for this regulation have remained less clear.

Here we have shown that by constraining the intermembrane distance after fusion pore opening to be ~5 nm or greater, calcium-bound Syt1 drives the nascent pore conductance to increase 2-3-fold relative to the low calcium case. This may also stabilize the pores against re-closure (71, 106). At intermediate calcium levels, the mean intermembrane distance is expected to have intermediate value, as the Syt1 molecules would be activated by calcium for a fraction of the time only. Thus, our results may explain why initial fusion pore size and its expansion rate increase as intracellular calcium increases (32, 37, 107, 108).

Our findings also recapitulate the observation that during exocytosis, fusion pore fluctuations increase with intracellular calcium (114). A mathematical model suggests that this originates in the cooperative mechanical effects of Syt1 and SNAREs which exert outward expansive forces on the fusion pore. These forces oppose the inward force that results from the intrinsic tendency of the protein-free fusion pore to close down due to membrane bending and tension effects (17). The net inward force is thus lowered, leading to a broader distribution of pore sizes and bigger fluctuations.

In neurons and many neuroendocrine cells, fusion is triggered by a brief calcium transient. The finding that fusion pore dilation is calcium sensitive suggests that the pore size and duration can be modulated by calcium dynamics. Thus, weak stimulations that result in brief calcium transients would be more likely to lead to small fusion pores and slow release, and strong stimulations would conversely result in larger and faster dilating pores. This behavior is indeed observed in neurons(9), and in neuroendocrine cells (7, 115). In this framework, different Syt isoforms would affect fusion pore dynamics differently, depending on their ability to reorient with respect to the membranes, their interactions with the SNAREs, and their calcium affinities.

MATERIALS AND METHODS

Recombinant protein expression and purification

All SNARE and Synaptotagmin-1 constructs used were generous gifts from James E. Rothman, unless noted otherwise. Plasmid pET32a-Trx-His6X-ApoE422K, used to express the N-terminal 22 kDa fragment of apolipoprotein E4 (residues 1–199, ApoE422K), was kindly provided by Dr Nicholas Fischer, Lawrence Livermore National Laboratory, CA (116, 117). Full-length VAMP2 (residues x1-116 in plasmid pET-SUMO-VAMP2) and ApoE422K were expressed and purified as previously described (16, 17). Rat Syt1 residues 96-421 corresponding to cytoplasmic C2AB domains were expressed from a pET28a-SUMO-synaptotagmin1 vector. $C2AB^{R398,399Q}$, $C2AB^{D309N}$ and $C2AB^{K326,327A}$ were generated from the wild-type sequence using the QuickChange site-directed mutagenesis kit (Stratagene, La Jolla, CA). $C2AB^{4W}$ and $C2AB^{4A}$ were prepared using QuikChange Multi Site-Directed Mutagenesis Kit (Stratagene, La Jolla, CA). Wild type C2AB and all mutated version of C2AB were expressed in BL21 (DE3) and purified as previously reported (62). Full length Syt1 (pET28a-SUMO-synaptotagmin 1, residues 57-421) was expressed in BL2 (DE3) at 37°C to optical density 0.8 (at 600 nm) and induced with 1 mM isopropyl β-D-thiogalactoside (IPTG) for 4 hours. Cells were then lysed by a cell disruptor (Avestin, Ottawa, CA) and lysates were clarified by centrifugation (35,000 rpm at 4°C for 30 min using a Beckman-Coulter Ti45 rotor and 70 ml polycarbonate tubes, corresponding to 142,160 × g). The supernatant was incubated with Ni-NTA agarose (Qiagen, Valencia, CA) overnight at 4°C. Protein bound beads were washed by buffer A (25 mM HEPES, pH 7.4, 400 mM KCl, 0.5 mM tris-2-carboxyethyl phosphine (TCEP)) supplemented with 50 mM imidazole and 1% Octylglucoside (OG). The protein was first separated from beads using buffer A supplemented with 400 mM Imidazole and 4% OG. Then the His-SUMO tag was cleaved by SUMO proteinase at 4°C for 2 hours. The protein was diluted 4 times by

dilution buffer (25 mM HEPES, 0.5 mM TCEP and 4% OG) and then immediately loaded into Mono S™ 5/50G column (GE Healthcare Bio-Sciences, Pittsburgh, PA). The full-length Syt1 was washed out by high salt buffer (25 mM HEPEs, 1 M KCl, 0.5 mM TCEP and 1% OG). After concentration determination using the Bradford assay (Bio Rad, Hercules, CA), the samples were aliquoted, flash frozen by plunging into liquid nitrogen, and stored at -80 °C for future use.

Reconstitution of synaptotagmin-1 and VAMP2 into nanodiscs

Eight copies of VAMP2 (~four per face) were incorporated into nanolipoprotein particles (vNLP8) as previously described (16, 17, 60). The protocol was modified to produce nanolipoprotein particles co-reconstituted with full-length Syt1 and VAMP2 (vsNLP). A mixture of palmitoyl-2-oleoylphosphatidylcholine (POPC) and 1,2-dioleoyl phosphatidylserine (DOPS) (85:15 molar ratio) dissolved in a chloroform-methanol mixture (2:1 by volume) was dried under nitrogen flow, then placed under vacuum for 2 hrs. All lipids were purchased from Avanti Polar Lipids (Alabaster, AL). The lipid film was re-suspended in 25 mM HEPES, pH 7.4, 140 mM KCl, 1 mM TCEP buffer with 1% OG supplemented by the desired amount of full length syt1 and VAMP2. The mixture was vortexed for 1 hr at room temperature followed by the addition of ApoE422K and vortexed for another half hour at room temperature and then 3 hours at cold room. The ApoE422K:VAMP2: syt1: lipid ratio for vsNLPs was 1:2:2:180. Excess detergent was removed using SM-2 bio-beads (Bio-Rad) overnight at 4°C with gentle shaking. The assembled vsNLPs were purified using size-exclusion chromatography using a Superose™ 6, 10/300 GL column (GE Healthcare Bio-Sciences, Pittsburgh, PA). Collected samples were concentrated using Amicon Ultra (30 KDa cutoff) centrifugal filter units, and analyzed by SDS-PAGE with Coomassie staining. The size distribution of the NLPs was determined for every batch of production using transmission electron microscopy (JEM-1400, JEOL, MA, USA). This allowed estimating the average number of ApoE copies per disc as before (17, 60), using previously published information about the number of ApoE copies as a function of disc size (117). The copy numbers of Syt1 and VAMP2 per disc were then estimated from the quantification of Syt1- or VAMP2-to-ApoE ratio using densitometry (ImageJ, NIH).

Stable flipped SNARE cell lines, PI(4,5)P_2 incorporation, and immunostaining

Stable "tCell" HeLa cell lines expressing flipped t-SNAREs (rat Syntaxin-1, residues 186-288, and rat SNAP-25, residues 2-206) and the nuclear marker CFP-nls (cyan fluorescent protein fused to nuclear localization signal) were a generous gift from the Rothman laboratory (118) and cultured as previously reported (16, 17). Briefly, the cells were cultured in DMEM (4500 mg/L glucose, L-glutamine, sodium pyruvate and sodium bicarbonate) and 10% (v/v) fetal calf serum at 37°C.

Where indicated, short-chain diC8-PI(4,5)P_2 (Echelon Biosciences Inc., Salt Lake City, UT) (1 mM stock solution, dissolved in water), was added to the cell culture medium to a final concentration of 20 μM and incubated 20 min at 37°C. Cells were then washed three times using extracellular buffer (ECS: 125 mM NaCl, 4 mM KCl, 2 mM $CaCl_2$, 1 mM $MgCl_2$, and 10 mM HEPES, pH adjusted to 7.2 with NaOH and 10 mM glucose added freshly).

For assessing diC8-PI(4,5)P_2 incorporation into the outer leaflet of the plasma membrane and lifetime, after 20 min incubation with the lipid, cells were rinsed thoroughly with phosphate buffered saline (PBS) supplemented with 10% goat serum, and kept at 37 ºC with the same solution for different durations. Mouse monoclonal anti-PI(4,5)P_2 primary antibodies (Echelon Biosciences Inc., Utah) were added to the cells at time points of 0, 40, and 80 minutes and incubated 1 hr at 37 °C. Then cells were fixed with 4% paraformaldehyde (Electron Microscopy Sciences, PA) for 20 min at room temperature before addition of goat anti-mouse IgM heavy chain secondary antibody conjugated with Alexa Fluor 647. Control cells that

were not incubated with diC8-PI(4,5)P_2 were treated similarly and fixed by 4% paraformaldehyde. Some cells were then permeabilized by 0.5% saponin (Sigma, MO) to allow access of the antibody to the inner leaflet of the plasma membrane where endogenous PI(4,5)P_2 resides. Cells were blocked for 30 min with PBS supplemented with 10% goat serum, followed by incubation with anti-PI(4,5)P_2 primary antibody for 1 hour at 37°C. After three successive washes in PBS, cells were incubated with the secondary antibody as above. All groups of cells were washed three times with PBS and mounted on a glass slide with mounting medium (ProLong Gold Antifade Mountant with DAPI, Molecular Probes, OR). Fluorescence images were collected using a spinning disk confocal microscope (model TiE, Nikon, Japan, equipped with a Yokogawa CSU-W1 spinning disc head and CFI Plan Apochromat Lambda 60x/1.4 oil immersion objective). Images were analyzed using ImageJ software. We drew a region of interest (ROI) around cells using the freehand ROI tool and measured the mean pixel intensity in the ROI. We then subtracted the intensity from a nearby region not containing any cells to define the background subtracted pixel intensity to define ΔF in Fig. 1B. For each condition, 10 regions of interest encompassing cells were analyzed from 3-6 independent preparations.

Single fusion pore conductance assay

All recordings were done as previously described (16, 17). Briefly, a dish with cultured tCells was rinsed using ECS, then mounted on a Thermo-Plate (Tokai Hit, Shizuoka-ken, Japan) pre-set to 37°C. tCells were visualized with an inverted Olympus IX71 microscope (Olympus Corp., Waltham, MA) using a ThorLabs USB3.0 digital camera (UI-3240CP-NIR-GL-TI) controlled by ThorCam software (ThorLabs, Newton, NJ). Recording pipettes (borosilicate glass, BF 150-86-10, Sutter Instruments, Novato, CA) were pulled using a model P-1000 pipette puller (Sutter Instruments, Novato, CA) and polished using a micro-forge (MF-830, Narishige, Tokyo, Japan). The pipette solution (PipSol) contained: 125 mM NaCl, 4 mM KCl, 1 mM MgCl2, 10 mM HEPES, 26 mM TEA-Cl, 2 mM ATP (freshly added), 0.5 mM EGTA, pH adjusted to 7.2 by NaOH and the indicated free calcium (0-100 μM) was adjusted by 0.1 M Calcium Standard Solutions (Thermo Fisher Scientific, Waltham, MA) and calculated using WEBMAXC STANDARD software (https://web.stanford.edu/~cpatton/webmaxcS.htm). The pipette was pre-filled by PipSol and then back filled with PipSol supplemented with nanodiscs with or without additional C2AB. All voltage-clamp recordings were made using a HEKA EPC10 Double USB amplifier (HEKA Elektronik Dr. Schulze GmbH, Lambrecht/Pfalz, Germany), controlled by Patchmaster software (HEKA). Current signals were digitized at 20 kHz and filtered at 3 kHz. The recording traces were exported to MatLab (MathWorks, Natick, MA) and analyzed as previously described in detail (16, 17).

Statistical analysis

Statistical analyses were performed using the two-sample t-test or the Kolmogorov-Smirnov test where indicated, using Matlab (MathWorks).

ACKNOWLEDGEMENTS

We thank Ekaterina Stroeva and Shyam Krishnakumar (Rothman Laboratory, Nanobiology Institute and Cell Biology, Yale University) for help with reconstitution of full-length Syt1 into nanodiscs. This work was supported by National Institute of General Medical Sciences of the National Institutes of Health under award numbers R01GM108954 (to EK) and R01GM117046 (to BOS). The content is solely the responsibility of the authors and does not necessarily represent the official views of the National Institutes of Health. We acknowledge computing resources from Columbia University's Shared Research Computing Facility project. We thank Zach McDargh for helpful discussions.

AUTHOR CONTRIBUTIONS

ZW and EK conceived the study and wrote the manuscript, with input from other co-authors. ND, ST and BO conceived the model, performed calculations, and contributed to the writing.

COMPETING INTERESTS

None

ADDITIONAL INFORMATION

SI Appendix

Correspondence and requests for materials should be addressed to B.O. bo8@columbia.edu or E.K. erdem.karatekin@yale.edu (lead contact).

FIGURE LEGENDS

Figure 1. Detection of single fusion pore currents mediated by Syt1 or its C2AB domain. **A**. Domain structures of the constructs used in this study. The structure of the soluble C2AB domains was rendered using PyMol, from PDB: 5kj7 (119). The orientations of the C2A and C2B domains relative to each other are not known in the presence of SNAREs and membranes. Conserved aspartate residues coordinating calcium ions are depicted in orange. Calcium ions are shown as orange spheres. A poly-lysine motif on the side of C2B (K324,K325,K326,K327 in the rat sequence) that preferentially interacts with $PI(4,5)P_2$ (80) is highlighted in cyan. **B**. Incorporation of exogenous $PI(4,5)P_2$ into the outer leaflet of flipped t-SNARE cells. Top: cells were incubated with diC8-$PI(4,5)P_2$ for 20 min, rinsed, and immunolabeled for $PI(4,5)P_2$ at the indicated time points. Only control cells that were permeabilized with saponin showed immunostaining, confirming absence of $PI(4,5)P_2$ in the outer leaflet, and providing a reference value for inner-leaflet $PI(4,5)P_2$ levels (a and b). Cells incubated with diC8-$PI(4,5)P_2$ showed immunofluorescence in the absence of permeabilization, indicating successful incorporation of $PI(4,5)P_2$ into the outer leaflet of the cell membrane (c-e). The signal was comparable to endogenous inner-leaflet $PI(4,5)P_2$ levels, and persisted at least for 80 min (lower panel). **C**. Schematic of the single-pore nanodisc-cell fusion assay. A glass micropipette forms a tight seal on a patch of the plasma membrane of a cell expressing "flipped" t-SNARE proteins on its surface. NLPs co-reconstituted with Syt1 and VAMP2 are included in the pipette solution (left). NLP-cell fusion results in a fusion pore connecting the cytosol to the cell's exterior (right). Under voltage clamp, direct-currents passing through the pore report pore dynamics. With ~25 nm NLPs, the scaffolding ring does not hinder pore expansion up to at least 10 nm diameter. Exogenous $PI(4,5)P_2$ can be added to the cell's outer leaflet as in B, and calcium in the pipette is controlled using calcium buffers. **D**. Representative currents that were recorded during vsNLP-tCell fusion, for the indicated conditions. $PI(4,5)P_2$ indicates cells were pre-treated with diC8-$PI(4,5)P_2$. Tetanus neurotoxin (TeNT) light chain cleaves VAMP2 and blocks exocytosis. Currents were larger when all components were present (SNAREs, Syt1, exogenous $PI(4,5)P_2$ and calcium). **E**. Similar to D, but instead of full-length

Syt1, 10 μM soluble Syt1 C2AB domains were used together with NLPs carrying ~4 copies of VAMP2 per face.

Figure 2. Syt1 promotes fusion and expands fusion pores in a calcium and PI(4,5)P_2 dependent manner, and soluble Syt1 C2AB recapitulates these effects. **A**. The rate at which current bursts appeared (pore nucleation rate) for the conditions indicated (error bars represent ± S.E.M.). SNARE-induced pores appeared more frequently in the presence of Syt1 or C2AB, when both calcium and PI(4,5)P_2 were also present. **B**. Mean single fusion pore conductance, $\langle G_{po} \rangle$, for different conditions as indicated (± S.E.M.). $\langle G_{po} \rangle$ was three-fold larger in the presence of Syt1 or C2AB, when both calcium and PI(4,5)P_2 were also present. **C**. Probability density functions (PDFs) for point-by-point open-pore conductances (see Methods) for pores induced in the presence of Syt1, PI(4,5)P_2 and with 0 or 100 μM calcium. Notice the higher density at larger conductance values in the presence of 100 μM calcium. **D**. Probability density functions for pore radii, calculated from the conductance PDFs in C, assuming a 15-nm long cylindrical pore (61). **E**. Apparent free energy profiles for Syt1 and soluble Syt1 C2AB domains in the absence or presence of calcium. These profiles were calculated from the pore radii PDFs as in D (see text and Methods) (17). The profiles were shifted vertically for clarity. **F**. Cumulative density functions (CDFs) for mean single-pore conductances for the conditions indicated. Soluble C2AB recapitulated effects of full-length Syt1 co-reconstituted into NLPs.

Figure 3. Pore expansion by Syt1 C2AB requires calcium, PI(4,5)P_2, and SNARE binding sites to be intact. **A**. Overview of the Syt1-SNARE complex (119). The electrostatic potential of PDB 5kj7 (119) was rendered using Pymol. The sites mutated in this work are marked by boxes labeled 1-3 on the left and shown in the panels to the right. D309 is a key calcium-binding residue (1), K326, K327 interact with acidic lipids (2), and R398,R399 interact with the t-SNAREs SNAP 25 (E51, E52 and E55) and syntaxin 1A (D231, E234 and E238). VAMP2 is shown in blue, SNAP25 in yellow, and syntaxin 1A in red. **B**. Mean single open-pore conductance values (+/- SEM) for the indicated conditions. Disrupting binding to calcium (D309N), acidic lipids (K326A, K327A), or the SNARE complex (R398, R399) resulted in ~3 fold smaller mean conductance compared to wild-type C2AB, largely or completely abrogating the effects of Syt1 C2AB. All conditions included 100 μM free calcium and pre-incubation of tCells with exogenous PI(4,5)P_2. **C**. Pore nucleation rate for the same conditions as in B. Pores appeared 2-3 times less frequently with the mutated proteins compared to wild-type Syt1 C2AB.

Figure 4. Calcium-dependence of pore properties. **A**. Mean single open-pore conductance, $\langle G_{po} \rangle$, as a function of free calcium concentration in the pipette solution. Plotted values are mean± S.E.M. A fit to a Hill equation $f(x) = \frac{a}{\left(\frac{K}{x}\right)^n + 1} + c$ is shown as the black line, where x=$[Ca^{2+}]_{free}$, n=2.3, and K=23 μM (see text). Best fit parameters (with 95% confidence bounds) were $a = 407.5\ (126.7, 688.3)$, $c = 173.3\ (2.683, 343.9)$, and $R^2 = 0.877$. **B**. Fusion pore open probability, P_o (fraction of time the pore is open during a burst), as a function of free calcium concentration (mean± S.E.M). **C**. Apparent free energy profiles, calculated as in Fig. 2E, for different calcium concentrations.

Figure 5. Calcium-induced membrane insertion of Syt1 C2AB hydrophobic loops are critical for both pore nucleation and expansion. **A**. Schematic depiction of Syt1 C2B domain's calcium-dependent interactions with membranes. Calcium-free C2B interacts with acidic lipids through its poly-lysine motif (highlighted in cyan as in Fig. 1). Upon binding to calcium, hydrophobic residues (V304 and I367 on C2B) insert into the membrane, causing C2B to reorient (41) and inducing membrane curvature (52, 53). In the presence of PI(4,5)P_2, the calcium-bound C2B assumes a tilted conformation with respect to the membrane (92). M173 and F234 on C2A top loops similarly insert into membranes in a calcium-

dependent manner, with similar effect on orientation and curvature generation (41) (not shown). A mutant with the membrane-inserting residues replaced with tryptophans (M173W, F234W, V304W and I367W, "4W") binds membranes more avidly, resulting in more membrane tubulation activity, whereas alanine substitution of the same residues ("4A") abolishes membrane penetration and curvature induction (52). **B.** Pore nucleation rate (mean ± S.E.M) in the presence of wildtype, 4W and 4A mutants. **C**. Mean open-pore conductance (± S.E.M) for the conditions indicated. **D**. Cumulative density functions for mean open-pore conductances for wild-type Syt1 C2AB, 4W and 4A mutants. In A, calcium-free C2B was rendered from PDB 5w5d (77) and calcium-bound C2B was rendered from 5kj7 (119).

Figure 6. Mathematical model of the fusion pore in the presence of Syt1 and SNAREs suggests a mechanical calcium-triggered pore dilation mechanism. **(A)** Schematic of model. The membrane free energy has contributions from membrane tension and bending energy. SNARE complexes may be unzippered and free to roam laterally, or zippered and confined to the pore waist. Crowding among zippered SNARE complexes generates entropic forces that tend to enlarge the pore (top view, shown lower right). The Syt1 C2B domain (green ellipsoid) has a SNARE-binding region, a polybasic patch and Ca^{2+}-binding loops. **(B)** The C2B calcium-binding loops may either be unburied (top panel) or buried (lower panel) in the membrane. In the buried state the SNARE complex tilts upwards, forcing the distance between the membranes to exceed a minimum value. The membrane separation constraint (and hence pore size constraint) is evaluated using the SNARE-C2B complex crystal structure in a space filling representation. VAMP2, syntaxin, SNAP25 and the C2B domain are shown blue, red, yellow and green, respectively. The C2B hydrophobic membrane-inserting residues (V304, I367), polybasic patch (K326, K327) and SNARE binding region (R398, R399) are shown orange, cyan and purple, respectively. The protein structure was generated with PyMOL (120) using the SNARE-C2B crystal structure (PDB ID 5ccg) (76). The TMD of the SNARE complex (PDB ID 3hd7) (121) was incorporated using UCSF chimera software (122). **(C)** Model-predicted free energy and experimental apparent free energy versus pore radius without calcium and in the presence of excess calcium. **(D)** Model-predicted normalized conductances shown with experimentally measured values for comparison. (**E)** Pore dilation mechanism emerging from the model. Without calcium the C2B domain is unburied, the SNARE complex lies parallel to the membrane and the membrane separation is set by the maximum thickness of the SNARE-C2B complex. With calcium, the calcium binding loops penetrate the plasma membrane, rotating the C2B domain and the entire SNARE-C2B complex which exerts force (red arrows) on the upper and lower membranes of the fusion pore in a lever-like action. These forces increase the fusion pore height, which is coupled by membrane energetics to fusion pore dilation.

REFERENCES

1. Brunger AT, Choi UB, Lai Y, Leitz J, & Zhou Q (2018) Molecular Mechanisms of Fast Neurotransmitter Release. *Annu Rev Biophys* 47:469-497.
2. Karatekin E (2018) Toward a unified picture of the exocytotic fusion pore. *FEBS Lett* 592(21):3563-3585.
3. Sharma S & Lindau M (2018) The fusion pore, 60 years after the first cartoon. *FEBS Lett* 592(21):3542-3562.
4. Chang CW, Chiang CW, & Jackson MB (2017) Fusion pores and their control of neurotransmitter and hormone release. *J Gen Physiol* 149(3):301-322.
5. Alabi AA & Tsien RW (2013) Perspectives on kiss-and-run: role in exocytosis, endocytosis, and neurotransmission. *Annu Rev Physiol* 75:393-422.
6. Collins SC*, et al.* (2016) Increased Expression of the Diabetes Gene SOX4 Reduces Insulin Secretion by Impaired Fusion Pore Expansion. *Diabetes* 65(7):1952-1961.
7. Fulop T, Radabaugh S, & Smith C (2005) Activity-dependent differential transmitter release in mouse adrenal chromaffin cells. *Journal of Neuroscience* 25(32):7324-7332.
8. He LM, Wu XS, Mohan R, & Wu LG (2006) Two modes of fusion pore opening revealed by cell-attached recordings at a synapse. *Nature* 444(7115):102-105.
9. Pawlu C, DiAntonio A, & Heckmann M (2004) Postfusional control of quantal current shape. *Neuron* 42(4):607-618.
10. Staal RGW, Mosharov EV, & Sulzer D (2004) Dopamine neurons release transmitter via a flickering fusion pore. *Nature Neuroscience* 7(4):341-346.
11. Chapochnikov NM*, et al.* (2014) Uniquantal release through a dynamic fusion pore is a candidate mechanism of hair cell exocytosis. *Neuron* 83(6):1389-1403.
12. Gandhi SP & Stevens CF (2003) Three modes of synaptic vesicular recycling revealed by single-vesicle imaging. *Nature* 423(6940):607-613.
13. Lisman JE, Raghavachari S, & Tsien RW (2007) The sequence of events that underlie quantal transmission at central glutamatergic synapses. *Nat Rev Neurosci* 8(8):597-609.
14. Verstreken P*, et al.* (2002) Endophilin mutations block clathrin-mediated endocytosis but not neurotransmitter release. *Cell* 109(1):101-112.
15. Bao H*, et al.* (2018) Dynamics and number of trans-SNARE complexes determine nascent fusion pore properties. *Nature* 554(7691):260-263.
16. Wu Z*, et al.* (2016) Nanodisc-cell fusion: control of fusion pore nucleation and lifetimes by SNARE protein transmembrane domains. *Sci Rep* 6:27287.
17. Wu Z*, et al.* (2017) Dilation of fusion pores by crowding of SNARE proteins. *Elife* 6:e22964.
18. Wu Z, Thiyagarajan S, O'Shaughnessy B, & Karatekin E (2017) Regulation of Exocytotic Fusion Pores by SNARE Protein Transmembrane Domains. *Front Mol Neurosci* 10:315.
19. Han X, Wang CT, Bai JH, Chapman ER, & Jackson MB (2004) Transmembrane segments of syntaxin line the fusion pore of Ca2+-triggered exocytosis. *Science* 304(5668):289-292.
20. Bretou M, Anne C, & Darchen F (2008) A fast mode of membrane fusion dependent on tight SNARE zippering. *J Neurosci* 28(34):8470-8476.
21. Kesavan J, Borisovska M, & Bruns D (2007) v-SNARE actions during Ca(2+)-triggered exocytosis. *Cell* 131(2):351-363.
22. Dhara M*, et al.* (2016) v-SNARE transmembrane domains function as catalysts for vesicle fusion. *Elife* 5:e17571.
23. Ngatchou AN*, et al.* (2010) Role of the synaptobrevin C terminus in fusion pore formation. *Proc Natl Acad Sci U S A* 107(43):18463-18468.
24. Weber T*, et al.* (1998) SNAREpins: Minimal machinery for membrane fusion. *Cell* 92(6):759-772.
25. Fang QH*, et al.* (2008) The role of the C terminus of the SNARE protein SNAP-25 in fusion pore opening and a model for fusion pore mechanics. *P Natl Acad Sci USA* 105(40):15388-15392.

26. Acuna C, *et al.* (2014) Microsecond dissection of neurotransmitter release: SNARE-complex assembly dictates speed and Ca(2)(+) sensitivity. *Neuron* 82(5):1088-1100.
27. Gucek A, *et al.* (2016) Dominant negative SNARE peptides stabilize the fusion pore in a narrow, release-unproductive state. *Cell Mol Life Sci* 73(19):3719-3731.
28. Zhao Y, *et al.* (2013) Rapid structural change in synaptosomal-associated protein 25 (SNAP25) precedes the fusion of single vesicles with the plasma membrane in live chromaffin cells. *Proc Natl Acad Sci U S A* 110(35):14249-14254.
29. Segovia M, *et al.* (2010) Push-and-pull regulation of the fusion pore by synaptotagmin-7. *P Natl Acad Sci USA* 107(44):19032-19037.
30. Zhang Z, Hui EF, Chapman ER, & Jackson MB (2010) Regulation of Exocytosis and Fusion Pores by Synaptotagmin-Effector Interactions. *Molecular Biology of the Cell* 21(16):2821-2831.
31. Zhang ZJ, Zhang Z, & Jackson MB (2010) Synaptotagmin IV Modulation of Vesicle Size and Fusion Pores in PC12 Cells. *Biophysical Journal* 98(6):968-978.
32. Wang CT, Bai J, Chang PY, Chapman ER, & Jackson MB (2006) Synaptotagmin-Ca2+ triggers two sequential steps in regulated exocytosis in rat PC12 cells: fusion pore opening and fusion pore dilation. *J Physiol* 570(Pt 2):295-307.
33. Wang CT, *et al.* (2003) Different domains of synaptotagmin control the choice between kiss-and-run and full fusion. *Nature* 424(6951):943-947.
34. Wang CT, Lu JC, Chapman ER, Martin TFJ, & Jackson MB (2003) Synaptotagmin IV induces long-duration kiss-and-run exocytosis through small fusion pores. *Biophysical Journal* 84(2):209a-209a.
35. Wang CT, *et al.* (2001) Synaptotagmin modulation of fusion pore kinetics in regulated exocytosis of dense-core vesicles. *Science* 294(5544):1111-1115.
36. Bai J, Wang CT, Richards DA, Jackson MB, & Chapman ER (2004) Fusion pore dynamics are regulated by synaptotagmin*t-SNARE interactions. *Neuron* 41(6):929-942.
37. Lynch KL, *et al.* (2008) Synaptotagmin-1 utilizes membrane bending and SNARE binding to drive fusion pore expansion. *Mol Biol Cell* 19(12):5093-5103.
38. Rao TC, *et al.* (2014) Distinct fusion properties of synaptotagmin-1 and synaptotagmin-7 bearing dense core granules. *Mol Biol Cell* 25(16):2416-2427.
39. Lai Y, *et al.* (2013) Fusion pore formation and expansion induced by Ca2+ and synaptotagmin 1. *Proc Natl Acad Sci U S A* 110(4):1333-1338.
40. Geppert M, *et al.* (1994) Synaptotagmin I: a major Ca2+ sensor for transmitter release at a central synapse. *Cell* 79(4):717-727.
41. Chapman ER (2008) How does synaptotagmin trigger neurotransmitter release? *Annu Rev Biochem* 77:615-641.
42. Bhalla A, Tucker WC, & Chapman ER (2005) Synaptotagmin isoforms couple distinct ranges of Ca2+, Ba2+, and Sr2+ concentration to SNARE-mediated membrane fusion. *Mol Biol Cell* 16(10):4755-4764.
43. Bhalla A, Chicka MC, & Chapman ER (2008) Analysis of the synaptotagmin family during reconstituted membrane fusion. Uncovering a class of inhibitory isoforms. *J Biol Chem* 283(31):21799-21807.
44. Pinheiro PS, Houy S, & Sorensen JB (2016) C2-domain containing calcium sensors in neuroendocrine secretion. *J Neurochem* 139(6):943-958.
45. Volynski KE & Krishnakumar SS (2018) Synergistic control of neurotransmitter release by different members of the synaptotagmin family. *Curr Opin Neurobiol* 51:154-162.
46. Craxton M (2010) A manual collection of Syt, Esyt, Rph3a, Rph3al, Doc2, and Dblc2 genes from 46 metazoan genomes--an open access resource for neuroscience and evolutionary biology. *BMC Genomics* 11:37.
47. Sugita S, Shin OH, Han W, Lao Y, & Sudhof TC (2002) Synaptotagmins form a hierarchy of exocytotic Ca(2+) sensors with distinct Ca(2+) affinities. *EMBO J* 21(3):270-280.

48. Hui E, *et al.* (2005) Three distinct kinetic groupings of the synaptotagmin family: candidate sensors for rapid and delayed exocytosis. *Proc Natl Acad Sci U S A* 102(14):5210-5214.
49. Xu J, Mashimo T, & Sudhof TC (2007) Synaptotagmin-1, -2, and -9: Ca(2+) sensors for fast release that specify distinct presynaptic properties in subsets of neurons. *Neuron* 54(4):567-581.
50. Brunger AT, Leitz J, Zhou Q, Choi UB, & Lai Y (2018) Ca(2+)-Triggered Synaptic Vesicle Fusion Initiated by Release of Inhibition. *Trends Cell Biol* 28(8):631-645.
51. Sudhof TC (2013) Neurotransmitter Release: The Last Millisecond in the Life of a Synaptic Vesicle. *Neuron* 80(3):675-690.
52. Martens S, Kozlov MM, & McMahon HT (2007) How synaptotagmin promotes membrane fusion. *Science* 316(5828):1205-1208.
53. Hui EF, Johnson CP, Yao J, Dunning FM, & Chapman ER (2009) Synaptotagmin-Mediated Bending of the Target Membrane Is a Critical Step in Ca2+-Regulated Fusion. *Cell* 138(4):709-721.
54. Chernomordik LV & Kozlov MM (2008) Mechanics of membrane fusion. *Nature Structural & Molecular Biology* 15(7):675-683.
55. Kozlov MM, McMahon HT, & Chernomordik LV (2010) Protein-driven membrane stresses in fusion and fission. *Trends in Biochemical Sciences* 35(12):699-706.
56. Zhang Z, *et al.* (2011) Release mode of large and small dense-core vesicles specified by different synaptotagmin isoforms in PC12 cells. *Mol Biol Cell* 22(13):2324-2336.
57. Lynch KL & Martin TF (2007) Synaptotagmins I and IX function redundantly in regulated exocytosis but not endocytosis in PC12 cells. *J Cell Sci* 120(Pt 4):617-627.
58. Osterberg JR, *et al.* (2015) Membrane Docking of the Synaptotagmin 7 C2A Domain: Electron Paramagnetic Resonance Measurements Show Contributions from Two Membrane Binding Loops. *Biochemistry* 54(37):5684-5695.
59. Voleti R, Tomchick DR, Sudhof TC, & Rizo J (2017) Exceptionally tight membrane-binding may explain the key role of the synaptotagmin-7 C2A domain in asynchronous neurotransmitter release. *Proc Natl Acad Sci U S A* 114(40):E8518-E8527.
60. Bello OD, Auclair SM, Rothman JE, & Krishnakumar SS (2016) Using ApoE Nanolipoprotein Particles To Analyze SNARE-Induced Fusion Pores. *Langmuir* 32(12):3015-3023.
61. Hille B (2001) *Ion channels of excitable membranes* (Sinauer, Sunderland, Mass.) 3rd Ed pp xviii, 814 p.
62. Ma L, *et al.* (2017) Single-molecule force spectroscopy of protein-membrane interactions. *Elife* 6:e30493.
63. Perez-Lara A, *et al.* (2016) PtdInsP2 and PtdSer cooperate to trap synaptotagmin-1 to the plasma membrane in the presence of calcium. *Elife* 5:e15886.
64. Honigmann A, *et al.* (2013) Phosphatidylinositol 4,5-bisphosphate clusters act as molecular beacons for vesicle recruitment. *Nat Struct Mol Biol* 20(6):679-686.
65. Bai J, Tucker WC, & Chapman ER (2004) PIP2 increases the speed of response of synaptotagmin and steers its membrane-penetration activity toward the plasma membrane. *Nat Struct Mol Biol* 11(1):36-44.
66. Chang S, Trimbuch T, & Rosenmund C (2018) Synaptotagmin-1 drives synchronous Ca(2+)-triggered fusion by C2B-domain-mediated synaptic-vesicle-membrane attachment. *Nat Neurosci* 21(1):33-40.
67. Sakmann B & Neher E (2009) *Single-channel recording* (Springer, New York, NY) 2nd Ed pp xxii, 700 p.
68. Schiavo G, Matteoli M, & Montecucco C (2000) Neurotoxins affecting neuroexocytosis. *Physiol Rev* 80(2):717-766.
69. Jackson MB (2009) Minimum membrane bending energies of fusion pores. *J Membr Biol* 231(2-3):101-115.
70. Cohen FS & Melikyan GB (2004) The energetics of membrane fusion from binding, through hemifusion, pore formation, and pore enlargement. *J Membr Biol* 199(1):1-14.

71. D'Agostino M, Risselada HJ, Endter LJ, Comte-Miserez V, & Mayer A (2018) SNARE-mediated membrane fusion arrests at pore expansion to regulate the volume of an organelle. *EMBO J* 37(19).
72. Mackler JM, Drummond JA, Loewen CA, Robinson IM, & Reist NE (2002) The C(2)B Ca(2+)-binding motif of synaptotagmin is required for synaptic transmission in vivo. *Nature* 418(6895):340-344.
73. Shin OH, Xu J, Rizo J, & Sudhof TC (2009) Differential but convergent functions of Ca2+ binding to synaptotagmin-1 C2 domains mediate neurotransmitter release. *Proc Natl Acad Sci U S A* 106(38):16469-16474.
74. Nishiki T & Augustine GJ (2004) Dual roles of the C2B domain of synaptotagmin I in synchronizing Ca2+-dependent neurotransmitter release. *J Neurosci* 24(39):8542-8550.
75. Borden CR, Stevens CF, Sullivan JM, & Zhu Y (2005) Synaptotagmin mutants Y311N and K326/327A alter the calcium dependence of neurotransmission. *Mol Cell Neurosci* 29(3):462-470.
76. Zhou Q*, et al.* (2015) Architecture of the synaptotagmin-SNARE machinery for neuronal exocytosis. *Nature* 525(7567):62-67.
77. Zhou Q*, et al.* (2017) The primed SNARE-complexin-synaptotagmin complex for neuronal exocytosis. *Nature* 548(7668):420-425.
78. Xue M, Ma C, Craig TK, Rosenmund C, & Rizo J (2008) The Janus-faced nature of the C(2)B domain is fundamental for synaptotagmin-1 function. *Nat Struct Mol Biol* 15(11):1160-1168.
79. Park Y*, et al.* (2015) Synaptotagmin-1 binds to PIP(2)-containing membrane but not to SNAREs at physiological ionic strength. *Nat Struct Mol Biol* 22(10):815-823.
80. Radhakrishnan A, Stein A, Jahn R, & Fasshauer D (2009) The Ca2+ affinity of synaptotagmin 1 is markedly increased by a specific interaction of its C2B domain with phosphatidylinositol 4,5-bisphosphate. *J Biol Chem* 284(38):25749-25760.
81. Davis AF*, et al.* (1999) Kinetics of synaptotagmin responses to Ca2+ and assembly with the core SNARE complex onto membranes. *Neuron* 24(2):363-376.
82. Martens S & McMahon HT (2008) Mechanisms of membrane fusion: disparate players and common principles. *Nat Rev Mol Cell Biol* 9(7):543-556.
83. Chapman ER & Davis AF (1998) Direct interaction of a Ca2+-binding loop of synaptotagmin with lipid bilayers. *J Biol Chem* 273(22):13995-14001.
84. Rhee JS*, et al.* (2005) Augmenting neurotransmitter release by enhancing the apparent Ca2+ affinity of synaptotagmin 1. *Proc Natl Acad Sci U S A* 102(51):18664-18669.
85. Helfrich W (1973) Elastic properties of lipid bilayers: theory and possible experiments. *Z Naturforsch C* 28(11):693-703.
86. Chizmadzhev YA, Kuzmin PI, Kumenko DA, Zimmerberg J, & Cohen FS (2000) Dynamics of fusion pores connecting membranes of different tensions. *Biophys J* 78(5):2241-2256.
87. Jackson MB (2010) SNARE complex zipping as a driving force in the dilation of proteinaceous fusion pores. *J Membr Biol* 235(2):89-100.
88. Kozlov MM, Leikin SL, Chernomordik LV, Markin VS, & Chizmadzhev YA (1989) Stalk mechanism of vesicle fusion. Intermixing of aqueous contents. *Eur Biophys J* 17(3):121-129.
89. Gao Y*, et al.* (2012) Single reconstituted neuronal SNARE complexes zipper in three distinct stages. *Science* 337(6100):1340-1343.
90. Ma L*, et al.* (2015) Munc18-1-regulated stage-wise SNARE assembly underlying synaptic exocytosis. *Elife* 4:e09580.
91. Mostafavi H*, et al.* (2017) Entropic forces drive self-organization and membrane fusion by SNARE proteins. *Proc Natl Acad Sci U S A* 114(21):5455-5460.
92. Kuo W, Herrick DZ, & Cafiso DS (2011) Phosphatidylinositol 4,5-bisphosphate alters synaptotagmin 1 membrane docking and drives opposing bilayers closer together. *Biochemistry* 50(13):2633-2641.

93. Herrick DZ, Sterbling S, Rasch KA, Hinderliter A, & Cafiso DS (2006) Position of synaptotagmin I at the membrane interface: cooperative interactions of tandem C2 domains. *Biochemistry* 45(32):9668-9674.
94. Kuo W, Herrick DZ, Ellena JF, & Cafiso DS (2009) The calcium-dependent and calcium-independent membrane binding of synaptotagmin 1: two modes of C2B binding. *J Mol Biol* 387(2):284-294.
95. Chizmadzhev YA, Cohen FS, Shcherbakov A, & Zimmerberg J (1995) Membrane mechanics can account for fusion pore dilation in stages. *Biophys J* 69(6):2489-2500.
96. Ryham RJ, Ward MA, & Cohen FS (2013) Teardrop shapes minimize bending energy of fusion pores connecting planar bilayers. *Phys Rev E Stat Nonlin Soft Matter Phys* 88(6):062701.
97. Nanavati C, Markin VS, Oberhauser AF, & Fernandez JM (1992) The Exocytotic Fusion Pore Modeled as a Lipidic Pore. *Biophysical Journal* 63(4):1118-1132.
98. Chanturiya A, Chernomordik LV, & Zimmerberg J (1997) Flickering fusion pores comparable with initial exocytotic pores occur in protein-free phospholipid bilayers. *P Natl Acad Sci USA* 94(26):14423-14428.
99. Doreian BW, Fulop TG, Meklemburg RL, & Smith CB (2009) Cortical F-Actin, the Exocytic Mode, and Neuropeptide Release in Mouse Chromaffin Cells Is Regulated by Myristoylated Alanine-rich C-Kinase Substrate and Myosin II. *Molecular Biology of the Cell* 20(13):3142-3154.
100. Barg S*, et al.* (2002) Delay between fusion pore opening and peptide release from large dense-core vesicles in neuroendocrine cells. *Neuron* 33(2):287-299.
101. Hanna ST*, et al.* (2009) Kiss-and-run exocytosis and fusion pores of secretory vesicles in human beta-cells. *Pflugers Archiv-European Journal of Physiology* 457(6):1343-1350.
102. MacDonald PE, Braun M, Galvanovskis J, & Rorsman P (2006) Release of small transmitters through kiss-and-run fusion pores in rat pancreatic beta cells. *Cell Metab* 4(4):283-290.
103. Bretou M*, et al.* (2014) Cdc42 controls the dilation of the exocytotic fusion pore by regulating membrane tension. *Mol Biol Cell* 25(20):3195-3209.
104. Kozlov MM & Chernomordik LV (2015) Membrane tension and membrane fusion. *Curr Opin Struct Biol* 33:61-67.
105. Wen PJ*, et al.* (2016) Actin dynamics provides membrane tension to merge fusing vesicles into the plasma membrane. *Nat Commun* 7:12604.
106. D'Agostino M, Risselada HJ, Lurick A, Ungermann C, & Mayer A (2017) A tethering complex drives the terminal stage of SNARE-dependent membrane fusion. *Nature* 551(7682):634-638.
107. Hartmann J & Lindau M (1995) A novel Ca(2+)-dependent step in exocytosis subsequent to vesicle fusion. *FEBS Lett* 363(3):217-220.
108. Fernandez-Chacon R & Alvarez de Toledo G (1995) Cytosolic calcium facilitates release of secretory products after exocytotic vesicle fusion. *FEBS Lett* 363(3):221-225.
109. Scepek S, Coorssen JR, & Lindau M (1998) Fusion pore expansion in horse eosinophils is modulated by Ca2+ and protein kinase C via distinct mechanisms. *EMBO J* 17(15):4340-4345.
110. Rothman JE, Krishnakumar SS, Grushin K, & Pincet F (2017) Hypothesis - buttressed rings assemble, clamp, and release SNAREpins for synaptic transmission. *FEBS Lett* 591(21):3459-3480.
111. van den Bogaart G*, et al.* (2011) Synaptotagmin-1 may be a distance regulator acting upstream of SNARE nucleation. *Nat Struct Mol Biol* 18(7):805-812.
112. Seven AB, Brewer KD, Shi L, Jiang QX, & Rizo J (2013) Prevalent mechanism of membrane bridging by synaptotagmin-1. *Proc Natl Acad Sci U S A* 110(34):E3243-3252.
113. Lin CC*, et al.* (2014) Control of membrane gaps by synaptotagmin-Ca2+ measured with a novel membrane distance ruler. *Nat Commun* 5:5859.
114. Zhou Z, Misler S, & Chow RH (1996) Rapid fluctuations in transmitter release from single vesicles in bovine adrenal chromaffin cells. *Biophysical Journal* 70(3):1543-1552.

115. Cardenas AM & Marengo FD (2016) How the stimulus defines the dynamics of vesicle pool recruitment, fusion mode, and vesicle recycling in neuroendocrine cells. *J Neurochem* 137(6):867-879.
116. Morrow JA, Arnold KS, & Weisgraber KH (1999) Functional characterization of apolipoprotein E isoforms overexpressed in Escherichia coli. *Protein Expr Purif* 16(2):224-230.
117. Blanchette CD*, et al.* (2008) Quantifying size distributions of nanolipoprotein particles with single-particle analysis and molecular dynamic simulations. *J Lipid Res* 49(7):1420-1430.
118. Giraudo CG, Eng WS, Melia TJ, & Rothman JE (2006) A clamping mechanism involved in SNARE-dependent exocytosis. *Science* 313(5787):676-680.
119. Lyubimov AY*, et al.* (2016) Advances in X-ray free electron laser (XFEL) diffraction data processing applied to the crystal structure of the synaptotagmin-1 / SNARE complex. *Elife* 5:e18740.
120. Schrodinger, LLC (2015) The PyMOL Molecular Graphics System, Version 1.8.
121. Stein A, Weber G, Wahl MC, & Jahn R (2009) Helical extension of the neuronal SNARE complex into the membrane. *Nature* 460(7254):525-U105.
122. Pettersen EF*, et al.* (2004) UCSF Chimera--a visualization system for exploratory research and analysis. *J Comput Chem* 25(13):1605-1612.

SI APPENDIX

The neuronal calcium sensor Synaptotagmin-1 and SNARE proteins cooperate to dilate fusion pores mechanically

Zhenyong Wu[1,2], Nadiv Dharan[3], Sathish Thiyagarajan[3], Ben O'Shaughnessy[3,*], and Erdem Karatekin[1,2,4,5,*]

1 Department of Cellular and Molecular Physiology, Yale University, New Haven, CT

2 Nanobiology Institute, Yale University, West Haven, CT

3 Department of Chemical Engineering, Columbia University, New York, NY

4 Department of Molecular Biophysics and Biochemistry, Yale University, New Haven, CT

5 Centre National de la Recherche Scientifique, Paris, France

* Corresponding authors (bo8@columbia.edu and erdem.karatekin@yale.edu)

Lead contact: EK (erdem.karatekin@yale.edu)

MATHEMATICAL MODEL OF THE FUSION PORE WITH SNARES AND SYNAPTOTAGMIN-1

The fusion pore between the nanolipoprotein particle (NLP) and the tCell membrane is assumed to have a toroidal shape. The toroidal assumption for the fusion pore was also used in several previous theoretical studies (1-3). The pore radius is denoted by r_{po} and the pore height, defined to be the separation between the NLP and tcell membrane, is h. We assume that each side of the NLP contains N v-SNAREs and that all are available to associate with the t-SNAREs in the tCell membrane and contribute to pore expansion. Out of N SNAREs, N_{Z} denotes the number of fully zippered SNAREs. For a given set of values $(r_{\mathrm{po}}, h, N, N_{\mathrm{Z}})$ the total free energy of the fusion pore is

$$U_{\mathrm{tot}}(r_{\mathrm{po}}, h, N, N_{\mathrm{Z}}) = U_{\mathrm{mb}} + U_{\mathrm{hyd}} + U_{\mathrm{SNARE}}, \quad (1)$$

where U_{mb}, U_{hyd} and U_{SNARE} stand for the membrane energy of the pore, the energy due to hydration forces between the NLP and tCell membranes, and the free energy associated with the SNAREpins, respectively.

Each SNARE is bound to a Syt1 C2AB domain at the primary interface between the SNARE and the C2B domain (4). The C2AB domain calcium binding loops can be unburied or buried in the membrane with a probability that depends on calcium concentration (see *"calcium dependent pore conductance"* below). In the unburied state, the C2B polybasic patch is facing the tCell membrane and parallel to it (5). In this orientation the C2B-attached SNARE is also roughly parallel to the membrane, and a height constraint $h > h_{\mathrm{min}}$ is imposed by the SNARE-C2B complex, such that the pore height cannot fall below the maximum thickness of the SNARE-C2B complex, i.e. $h_{\mathrm{min}} = 3$ nm. In the buried state, the C2AB domain anchors to the membrane by insertion of its calcium binding loops ~1 nm into the membrane (6), and the polybasic patch is distanced ~0.5 nm from the membrane (7). With respect to the unburied state, this configuration has a rotated C2B domain, which is attached to the SNARE complex at the primary interface, such that the SNARE complex is somewhat raised above the membrane and is concomitantly tilted by ~ 15° with respect to the membrane plane (Figure 6B, main text). This tilt angle is measured by taking the inverse sine of the ratio between the SNARE motif length projected on the vertical axis of the pore and the length of the SNARE motif. Thus, the C2B domain acts as a fulcrum about which the SNARE lever pivots. This configuration imposes a larger pore height constraint in the C2AB buried state of $h_{\mathrm{min}} = 5.5$ nm.

We calculate the pore conductance in the absence of calcium where C2AB domains are unburied and in saturating calcium levels when all C2AB domain are buried, and use these values to predict the mean pore conductance as described in the subsection "*calcium dependent pore conductance"* below. The expressions for the different energy terms in eq. (1) are described below.

Membrane free energy

The NLP and tCell membranes are modelled as a planar bilayer with diameter D and an infinite planar bilayer, respectively, and both are at a constant surface tension. The membrane free energy of the toroidal fusion pore is the sum of two contributions

$$U_{\mathrm{mb}}(r_{\mathrm{po}}, h) = U_{\mathrm{bend}}(r_{\mathrm{po}}, h) + U_{\mathrm{tens}}(r_{\mathrm{po}}, h). \quad (2)$$

In eq. (2), $U_{\mathrm{bend}}(r_{\mathrm{po}}, h)$ is the membrane bending energy and $U_{\mathrm{tens}}(r_{\mathrm{po}}, h)$ is the energy due to tension. The former is given by (8)

$$U_{\mathrm{bend}}(r_{\mathrm{po}},h)=\frac{\kappa}{2}\int_{A_{\mathrm{mb}}}(2C)^2\,dA, \tag{3}$$

where κ is the membrane's bending modulus, C is the local mean curvature, and the integration is taken over the area of the membrane mid plane of the pore, A_{mb}. The free energy due to tension is

$$U_{\mathrm{tens}}(r_{\mathrm{po}},h)=\gamma\Delta A, \tag{4}$$

where γ is the membrane's tension and $\Delta A=A_{\mathrm{p}}-A_{\mathrm{rim}}$ is the difference between the pore area (A_{p}) and the area of both rims of the pore (A_{rim}) that must be removed from the NLP and the tCell membranes to form the pore. The integrals and areas were previously evaluated to give the following expression for the bending and tension energies

$$U_{\mathrm{bend}}(r_{\mathrm{po}},h)=\pi\kappa\left[\frac{2(R+H)^2}{H\sqrt{R(R+2H)}}\tan^{-1}\sqrt{\frac{R+2H}{R}}-4\right],$$
$$U_{\mathrm{tens}}(\mathrm{r}_{\mathrm{po}},h)=2\pi\gamma\{[(\pi-2)H+\pi R]H-(R+H)^2\} \tag{5}$$

where $H=(h+\delta)/2$, $R=r_{\mathrm{po}}+\delta/2$ and δ is the membrane thickness (1). We set the bending modulus to a typical value commonly used of $\kappa=20\ k_BT$ (9). We set the value of γ to 0.66 pN nm^{-1} , which was previously obtained as a best fit parameter in a similar experimental setup where fusion between the tCell and the NLP was induced by SNAREs alone (10)**.**

Short-ranged steric hydration free energy

The pressure due to short-ranged hydration forces between membranes with separation d follows the form $P_0\exp(-d/\lambda)$, where λ is the characteristic length scale over which the hydration forces decay and P_0 is a pressure pre-factor (11). The steric hydration free energy is evaluated by calculating the work done by the hydration pressure to increase the pore size and the membrane separation as was done in our previous work (10). The expression for the hydration free energy is given by

$$U_{\mathrm{hyd}}=P_0\lambda\left\{\left(\frac{\pi D^2}{4}\right)\exp\left(-\frac{h}{\lambda}\right)+\pi l\exp\left(-\frac{2r_{\mathrm{po}}}{\lambda}\right)\left(r_{\mathrm{po}}+\frac{\lambda}{2}\right)\right\}, \tag{6}$$

where $l=\sqrt{2\lambda(h+2\delta)}$ is the effective pore height that substantially contributes to the steric hydration interaction. The first term in eq. (6) gives the work done by the hydration forces to bring two distant planar membranes to a separation h, while the second term is the work done to separate the membranes to form a pore of radius r_{po}. Values for P_0 and λ are obtained from previous studies and are set to $P_0=5\times10^{11}$ dyn/cm^2 and $\lambda=0.1$ nm (see Table S1).

Free energy of SNAREs

We assume that each side of the NLP contains N v-SNAREs that are all available to associate with the t-SNAREs in the tCell membrane and contribute to pore expansion. SNAREs can be fully zippered, where their TMDs are circularly arranged near the fusion pore waist. Alternatively, they can adopt a partially zippered configuration, where the TMD and linker domain are unzippered, and the v-SNARE and t-SNARE TMDs are located on the NLP and tCell membranes, respectively, but on the same side of the fusion pore. We denote the number of fully and partially zippered as N_{Z} and N_{UZ}, respectively. The SNARE free energy in the fully zippered state reads

$$U_{\mathrm{Z}}(r_{\mathrm{po}}, N_{\mathrm{Z}}) = -N_{\mathrm{Z}} k_{\mathrm{B}} T \left[\ln \frac{2\pi r_{\mathrm{po}} - N_{\mathrm{Z}} b}{N_{\mathrm{Z}} b} + 1 \right] - N_{\mathrm{Z}} k_{\mathrm{B}} T \ln \Omega_{\mathrm{Z}} - N_{\mathrm{Z}} \epsilon_{\mathrm{Z}}, \quad (7)$$

where k_{B} is the Boltzmann constant, T is the temperature and $b = 2$ nm is the thickness of a single SNARE (10). The first term in eq. (7) is the positional entropy of the zippered SNAREs TMDs. The second term is the orientational entropy associated with the zippered SNAREs. We assume that these are stiff rods that can explore a small solid angle of $\Omega_{\mathrm{Z}} = 0.05$ sr, based on molecular dynamics studies of t-SNARE TMDs showing that these domains explore angles of 10° around their equilibrium position (12). We assume that for the zippered SNAREs the equilibrium orientation is the local normal to the fusion pore membrane. The last term is the total energy released when N_{Z} SNAREs fully zippered, where ϵ_{Z} is the zippering energy per SNARE.

The SNAREs free energy in the partially zippered state reads

$$U_{\mathrm{UZ}}(r_{\mathrm{po}}, N_{\mathrm{UZ}}) = -N_{\mathrm{UZ}} k_{\mathrm{B}} T \ln \frac{2\pi D}{b} - N_{\mathrm{UZ}} k_{\mathrm{B}} T \ln \Omega_{\mathrm{UZ}}. \quad (8)$$

The first term in eq. (8) is the positional entropy of the TMDs, while the second term is the orientational entropy associated with a solid angle Ω_{UZ} explored by the SNAREs. In the partially zippered state the SNARE linker domains are assumed to be unstructured, which allows them to adopt all orientations where they are not intersecting with the membranes. Since this orientational freedom is available when the SNAREs are away from the fusion pore, we restrict their position to the edge of the pore and set $\Omega = \Omega_{\mathrm{UZ}} = \pi$.

Total free energy as a function of pore size, minimum membrane separation, and total number of SNAREs

To obtain the free energy of a fusion pore with a radius r_{po}, we numerically summed all the Boltzmann factors of all possible states according to

$$\exp\left(-\frac{U_{\mathrm{tot}}(r_{\mathrm{po}}, h_{\mathrm{min}}, N)}{k_{\mathrm{B}} T}\right) = \sum_{N_{\mathrm{Z}}=0}^{N} \int_{h_{\mathrm{min}}}^{\infty} \exp\left(-\frac{U_{\mathrm{tot}}(r_{\mathrm{po}}, h, N, N_{\mathrm{Z}})}{k_{\mathrm{B}} T}\right) dh \quad (9)$$

where we set the number of SNAREs to $N = 4$ to match experiment.

Calcium dependent pore conductance

We calculate the pore conductance from the model predicted mean pore size and height using the simplifying cylindrical pore geometry approximation, as was done in the experiments (Table S2). The model predicted conductances in the absence of calcium, G_0, and in the excess of calcium (100 μM), G_{100}, were found to be $60\% - 70\%$ larger than experimentally measured; the ratio G_{100}/G_0 was close to that measured in the experiments. We compute the pore conductance as a function of calcium concentration as a weighted average between G_0 and G_{100} according to

$$G([\mathrm{Ca}^{2+}]) = G_{100} \cdot P([\mathrm{Ca}^{2+}]) + G_0 \cdot \left(1 - P([\mathrm{Ca}^{2+}])\right), \quad (10)$$

where $P([\mathrm{Ca}^{2+}])$ denotes the calcium dependent probability that the C2AB domain buries into the membrane. This probability amounts to the fraction of buried C2AB domain and , thus, can be described by the Hill equation (13, 14)

$$P([\mathrm{Ca}^{2+}]) = \frac{[\mathrm{Ca}^{2+}]^n}{[\mathrm{Ca}^{2+}]^n + [\mathrm{Ca}^{2+}]_{1/2}^n} \,. \qquad (11)$$

We set the Hill coefficient to $n = 2.3$ and the calcium concentration at which half of the Syt1 is buried in the membrane to $[\mathrm{Ca}^{2+}]_{1/2} = 23$ μM (**Table S1**), according to results obtained from liposome binding assays (15, 16).

We also calculated G_0 and G_{100} using a toroidally shaped pore as assumed by the model. This method resulted in values a factor ~4 larger than those experimentally measured, but the conductance ratio between the cases of saturating levels of calcium and absence of calcium was very similar to the ratio calculated using the cylindrical pore approximation (for the toroidal pore we find a conductance ratio of 2.01). The larger conductances predicted by the model, which are a reflection of larger model predicted pore sizes (Table S2), may be attributed to effects not included in the model, such as adhesive interactions between the membranes (17) and/or differences in lipid density and composition between the two leaflets that may disfavor pore expansion (18).

SUPPLEMENTARY TABLE 1

Symbol	Meaning	Value	Legend
$\boldsymbol{\delta}$	Membrane thickness	5 nm	(A)
$\boldsymbol{\epsilon_Z^0}$	Zippering energy of SNARE's linker and TMD domains	9.6 k_BT	(B)
$\boldsymbol{D}$	NLP diameter	24 nm	(C)
$\boldsymbol{\lambda}$	Hydration interactions decay length	0.1 nm	(B)
$\boldsymbol{P_0}$	Pressure pre-factor for steric hydration interaction	5×10^{11} dyn/cm^2	(D)
$\boldsymbol{\kappa}$	Membrane bending modulus	20 k_BT	(E)
$\boldsymbol{\gamma}$	Membrane tension	0.66 pN · nm^{-1}	(B)
$\boldsymbol{\Omega_Z}$	Solid angle explored by fully zippered SNAREs	0.05 sr	(F)
$\boldsymbol{[Ca^{2+}]_{1/2}}$	Apparent affinity of Syt1 to calcium in the presence of PIP2 containing membranes	23 μM	(G)
$\boldsymbol{n}$	Hill coefficient	2.3	(G)

Table S1. Parameters used in the mathematical model with coarse-grained membranes, SNAREs and Synaptotagmin-1 C2B domains. (A) Measured in (19). (B) Estimated previously as a best fit model parameter to experiments where NLP-tCell fusion pore was induced only by SNAREs (10). (C) Consistent with NLP diameter measurements in this study. (D) Calculated as the weighted average of the hydration pressures of palmitoyl-2-oleoyl phosphatidylcholine (POPC) and 1,2-dioleoyl phosphatidylserine (DOPS) adopted from (11), using a (85:15) molar ratio of POPC:DOPS as present in the NLP in the current study. (E) Values for the bending modulus range between $10 - 50\ k_BT$ (20-23). We used a common value of $\kappa = 20\ k_BT$ (9). (F) Calculated based on a 10° angle explored by t-SNARE TMDs around the equilibrium configuration, as measured in molecular dynamics simulations (12). (G) Measured in Syt1-liposome binding assays (14, 15)

SUPPLEMENTARY TABLE 2

	Mean pore conductance (pS)		Mean pore radius (nm)		Conductance ratio
	0 μM calcium	100 μM calcium	0 μM calcium	100 μM calcium	
Model	404.15 ± 25.82	942.28 ± 61.03	1.06 ± 0.51	1.71 ± 0.55	2.33 ± 0.36
Experiments	246.59 ± 33.86	554.98 ± 65.84	0.84 ± 0.06	1.26 ± 0.07	2.26 ± 0.41

Table S2: Comparison of pore conductances between model and experiments. All model errors are S.D. Experimental errors are S.E.M.

SUPPLEMENTARY FIGURE LEGENDS

Figure S1. Co-reconstitution of Synaptotagmin-1 and VAMP2 into nanolipoprotein particles (vsNLPs). **A**. Schematic of an NLP reconstituted with 4 copies per face each with Syt1 and VAMP2. Syt1 C2AB domains are shown in green; VAMP2 is shown in blue and the scaffold protein ApoE protein is shown in cyan. Domain structures of Syt1 and VAMP2 are indicated. **B**. Typical size-exclusion chromatography elution profiles of vNLP (NLPs loaded with VAMP2 alone) and vsNLP (NLPs loaded with VAMP2 and Syt1) samples using a Superose 6 Increase 10/300 GL column. Proteins were detected using absorbance at 280 nm. Collected eluted volumes are indicated by horizontal bars above each profile. **C**. SDS-PAGE stained with Coomassie Brilliant Blue shows the purified NLPs carried Syt1 and VAMP2 proteins. **D**. A representative transmission electron microscopy (TEM) image of a vsNLP sample after purification. Nanodiscs indicated by white stars have their lipid bilayer plane positioned perpendicularly to the imaging plane. **E**. Distribution of vsNLP sizes from TEM images. More dilute samples (5-10x) than the example shown in D were used for size quantification, such that most NLPs were lying flat on the grid. A Gaussian fit to the distribution is shown as the red solid line (fitted mean diameter = 25±5.6 nm (± SD), n = 200 NLPs). **F-H.** Characterization of nanolipoprotein particles reconstituted with VAMP2 alone. **F**. SDS-PAGE of purified vNLPs stained with Coomassie Brilliant Blue indicting the NLPs incorporated ApoE and VAMP2 proteins. **G**. Negative stain transmission electron microscopy image of a representative vNLP sample. Nanodiscs indicated by white stars are oriented with their disc plane perpendicular to the imaging plane. **H**. Size distribution of vNLPs reconstituted with a total of 8 copies of VAMP2 per disc. A Gaussian fit is shown as the red solid line (best fit diameter =25 ± 4.6 nm (mean ± SD), 171 discs were analyzed).

Figure S2. Additional properties of single fusion pores in the presence of full-length Syt1 or soluble C2AB. Open-pore conductance fluctuations relative to mean (**A**), average flicker rate during a burst (**B**), average open-pore probability, P_o, during a current burst (fraction of time pore is in the open state during a burst) (**C**), and average burst lifetime, T_o, (**D**) for the indicated conditions. **E**. Distributions of the number of flickers per burst, $N_{flickers}$, for the indicated conditions. Fits to geometric distributions are shown in red, $y = p(1-p)^n,\ n = 0, 1, 2, 3, \ldots$. Best fit parameters (with $\pm$ 95% confidence intervals) are $p = 0.08 \pm 0.008$ (no Syt1, 100 μM Ca^{2+}, averaged over 49 individual fusion pores from 10 cells), 0.11 ± 0.022 (Syt1, 0 μM Ca^{2+}; averaged over 24 individual fusion pores from 11 cells), 0.09 ± 0.005 (Syt1, 100 μM Ca^{2+}; averaged over 123 individual fusion pores from 20 cells). **F**. Distribution of burst

lifetimes, T_o for the indicated conditions. Best fits to single exponentials are shown as red curves, with means (and 95% confidence intervals) as follows. No Syt1, 100 μM Ca^{2+}: 6.1 s (4.7 to 8.3 s, 49 fusion pores from 10 cells), Syt1, 0 μM Ca^{2+}: 6.5 s (4.5 to 10.1 s, 24 fusion pores from 11 cells), Syt1, 100 μM Ca^{2+}: 16 s (13.5 to 19.3 s, 123 fusion pores from 20 cells).

Figure S3. Syt1 C2AB dilates fusion pores in a calcium and $PI(4,5)P_2$ dependent manner. **A-D**. Probability density function (PDF) for point-by-point open-pore conductance values for the indicated conditions. Substantial density is present for $Gpo \gtrsim 500$ pS only when C2AB, calcium, and $PI(4,5)P_2$ were all present. **F-I**. PDFs for open-pore radii corresponding to the conductance distributions in A-D, assuming pores are 15 nm long cylinders. Data were from 49 fusion pores/10 cells (SNARE only), 44 fusion pores/12 cells (0 μM Ca^{2+}), 84 fusion pores/19 cells (no $PI(4,5)P_2$) and 98 fusion pores/17 cells (100 μM Ca^{2+} plus $PI(4,5)P_2$).

Figure S4. Additional fusion pore properties for Syt1 C2AB domains carrying mutations in D309, K326-327 and R398-399. **A**. Open-pore conductance fluctuations relative to mean. Compared with the SNARE-alone (no C2AB) group, fluctuations were larger for wild-type C2AB, and lower for $C2AB^{K326A,327A}$. **B**. Average flicker rate for the same conditions as in A. Compared with the SNARE alone group (no C2AB), C2AB, $C2AB^{K326A,K327A}$ and $C2AB^{R398Q,R399Q}$ decreased the flicker rate. **C**. Average pore open probability during a burst, P_o, for the indicated conditions. Compared with the SNARE alone group (no C2AB), C2AB, $C2AB^{K326A,K327A}$ and $C2AB^{R398Q,R399Q}$ had larger pore open probabilities. **D**. Average burst lifetimes for the same conditions. Error bars are +/- S.E.M. *, *** indicate $p < 0.05$ and $p < 0.001$, respectively, using the Kolmogorov-Smirnov test, compared with the SNARE alone group. Data were from no C2AB: 49 pores/10 cells, C2AB: 98 pores/17 cells, $C2AB^{K326A,327A}$: 42 pores/14 cells, $C2AB^{D309N}$ (18 pores/7 cells), $C2AB^{R398Q,R399Q}$ (42 pores/18 cells).

Figure S5. Additional fusion pore properties as a function of free calcium concentration, $[Ca^{2+}]_{free}$. **A-C**. Average single-pore conductance fluctuations relative to mean (**A**), average burst lifetime (**B**), average flicker rate (**C**) as a function of $[Ca^{2+}]_{free}$. Error bars are +/- S.E.M. **D**. Probability density functions (PDFs) for point-by-point open-pore conductance values at different $[Ca^{2+}]_{free}$. The probability density for $G_{po} \gtrsim 500$ pS increases as a function of calcium. (0 μM Ca^{2+}: 44 pores/12 cells; 5 μM Ca^{2+}: 54 pores/20 cells; 20 μM Ca^{2+}: 114 pores/18 cells; 50 μM Ca^{2+}: 88 pores/26 cells; 100 μM Ca^{2+}: 98 pores/17 cells).

Figure S6. Additional fusion pore properties for Syt1 C2AB membrane penetration mutants. **A-D**. Average single-pore conductance fluctuations relative to mean (**A**), burst lifetime (**B**), pore open probability during a burst, P_o (**C**), and flicker rate (**D**) for SNAREs alone (no C2AB), wild-type Syt1 C2AB (C2AB), the 4W mutant with enhanced membrane-penetration ability (M173W, F234W, V304W and I367W), and the 4A mutant which cannot penetrate membranes in response to calcium (M173A, F234A, V304A and I367A). Error bars are +/- S.E.M. **E**. Probability density functions (PDFs) for point-by-point open-pore conductance values for wild-type C2AB, and the membrane penetration mutants 4A and 4W. (4W: 115 pores/20 cells, 4A: 31 pores/9 cells)

Figure S7. Results of the mathematical model of the toroidal fusion in the presence of SNAREs and Syt1 C2AB domains. **(A)** Pore height, defined as the maximal separation between the NLP and the tCell membranes, as a function of pore radius in the absence an excess of calcium. **(B)** Mean number of fully zippered SNAREs as a function of pore radius.

REFERENCES

1. Chizmadzhev YA, Kuzmin PI, Kumenko DA, Zimmerberg J, & Cohen FS (2000) Dynamics of fusion pores connecting membranes of different tensions. *Biophys J* 78(5):2241-2256.
2. Jackson MB (2010) SNARE complex zipping as a driving force in the dilation of proteinaceous fusion pores. *J Membr Biol* 235(2):89-100.
3. Kozlov MM, Leikin SL, Chernomordik LV, Markin VS, & Chizmadzhev YA (1989) Stalk mechanism of vesicle fusion. Intermixing of aqueous contents. *Eur Biophys J* 17(3):121-129.
4. Zhou Q*, et al.* (2015) Architecture of the synaptotagmin-SNARE machinery for neuronal exocytosis. *Nature* 525(7567):62-67.
5. Kuo W, Herrick DZ, Ellena JF, & Cafiso DS (2009) The calcium-dependent and calcium-independent membrane binding of synaptotagmin 1: two modes of C2B binding. *J Mol Biol* 387(2):284-294.
6. Herrick DZ, Sterbling S, Rasch KA, Hinderliter A, & Cafiso DS (2006) Position of synaptotagmin I at the membrane interface: cooperative interactions of tandem C2 domains. *Biochemistry* 45(32):9668-9674.
7. Kuo W, Herrick DZ, & Cafiso DS (2011) Phosphatidylinositol 4,5-bisphosphate alters synaptotagmin 1 membrane docking and drives opposing bilayers closer together. *Biochemistry* 50(13):2633-2641.
8. Helfrich W (1973) Elastic properties of lipid bilayers: theory and possible experiments. *Z Naturforsch C* 28(11):693-703.
9. Jackson MB (2009) Minimum membrane bending energies of fusion pores. *J Membr Biol* 231(2-3):101-115.
10. Wu Z*, et al.* (2017) Dilation of fusion pores by crowding of SNARE proteins. *Elife* 6:e22964.
11. Rand R & Parsegian V (1989) Hydration forces between phospholipid bilayers. *Biochimica et Biophysica Acta -Reviews on Biomembranes* 988(3):351-376.
12. Knecht V & Grubmüller H (2003) Mechanical coupling via the membrane fusion SNARE protein syntaxin 1A: a molecular dynamics study. *Biophys J* 84(3):1527-1547.
13. Radhakrishnan A, Stein A, Jahn R, & Fasshauer D (2009) The Ca2+ affinity of synaptotagmin 1 is markedly increased by a specific interaction of its C2B domain with phosphatidylinositol 4,5-bisphosphate. *J Biol Chem* 284(38):25749-25760.
14. Bai J, Wang CT, Richards DA, Jackson MB, & Chapman ER (2004) Fusion pore dynamics are regulated by synaptotagmin*t-SNARE interactions. *Neuron* 41(6):929-942.
15. Bai J, Tucker WC, & Chapman ER (2004) PIP2 increases the speed of response of synaptotagmin and steers its membrane-penetration activity toward the plasma membrane. *Nat Struct Mol Biol* 11(1):36-44.
16. Davis AF*, et al.* (1999) Kinetics of synaptotagmin responses to Ca2+ and assembly with the core SNARE complex onto membranes. *Neuron* 24(2):363-376.
17. Long R, Hui CY, Jagota A, & Bykhovskaia M (2012) Adhesion energy can regulate vesicle fusion and stabilize partially fused states. *J R Soc Interface* 9(72):1555-1567.
18. D'Agostino M, Risselada HJ, Endter LJ, Comte-Miserez V, & Mayer A (2018) SNARE-mediated membrane fusion arrests at pore expansion to regulate the volume of an organelle. *EMBO J* 37(19).
19. Mitra K, Ubarretxena-Belandia I, Taguchi T, Warren G, & Engelman DM (2004) Modulation of the bilayer thickness of exocytic pathway membranes by membrane proteins rather than cholesterol. *Proc Natl Acad Sci U S A* 101(12):4083-4088.
20. Brochard F & Lennon JJJdP (1975) Frequency spectrum of the flicker phenomenon in erythrocytes. 36(11):1035-1047.
21. Khelashvili G, Kollmitzer B, Heftberger P, Pabst G, & Harries D (2013) Calculating the Bending Modulus for Multicomponent Lipid Membranes in Different Thermodynamic Phases. *J Chem Theory Comput* 9(9):3866-3871.

22. Marsh D (2006) Elastic curvature constants of lipid monolayers and bilayers. *Chem Phys Lipids* 144(2):146-159.
23. Cohen FS & Melikyan GB (2004) The energetics of membrane fusion from binding, through hemifusion, pore formation, and pore enlargement. *J Membr Biol* 199(1):1-14.

Figure 1

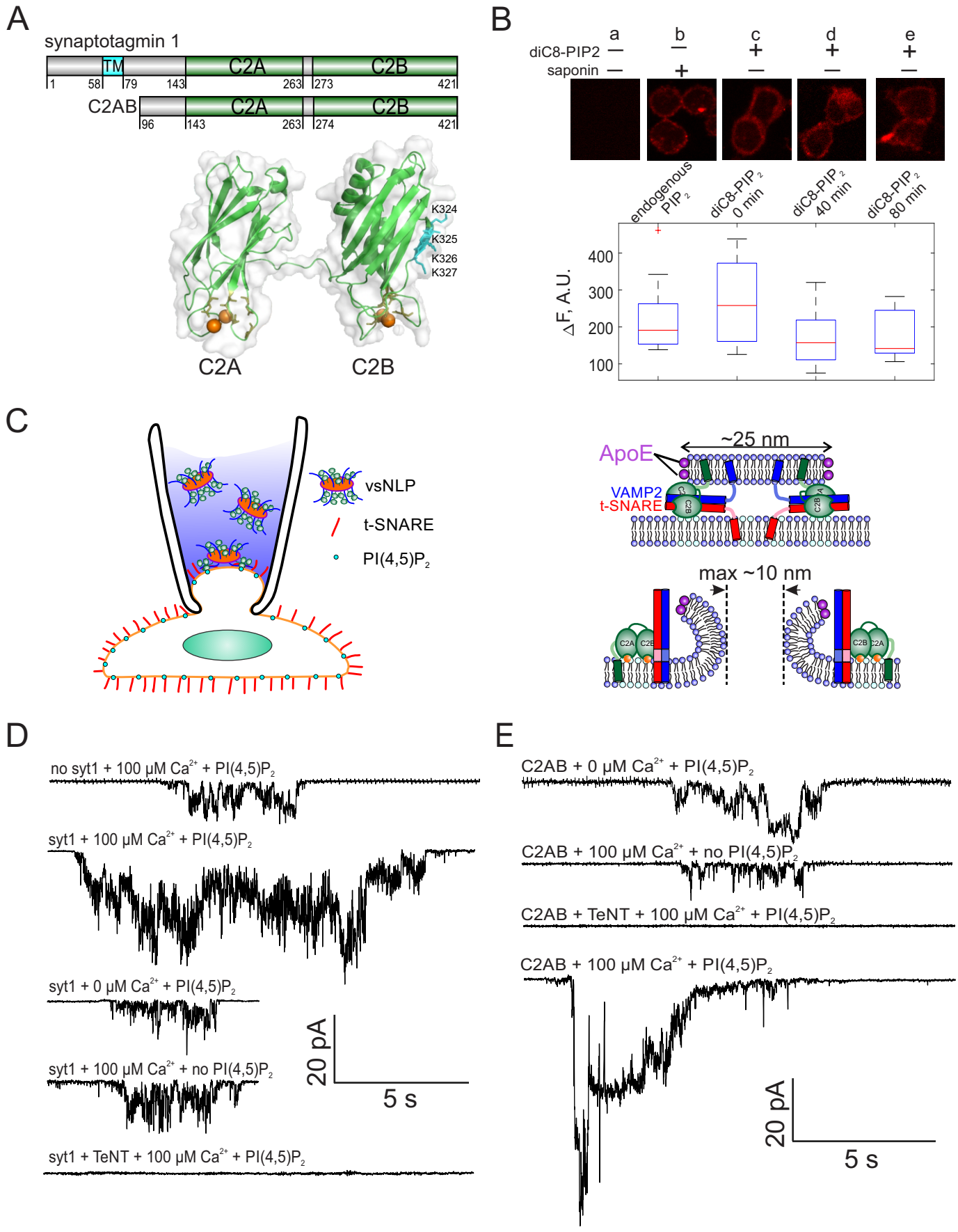

Figure 2

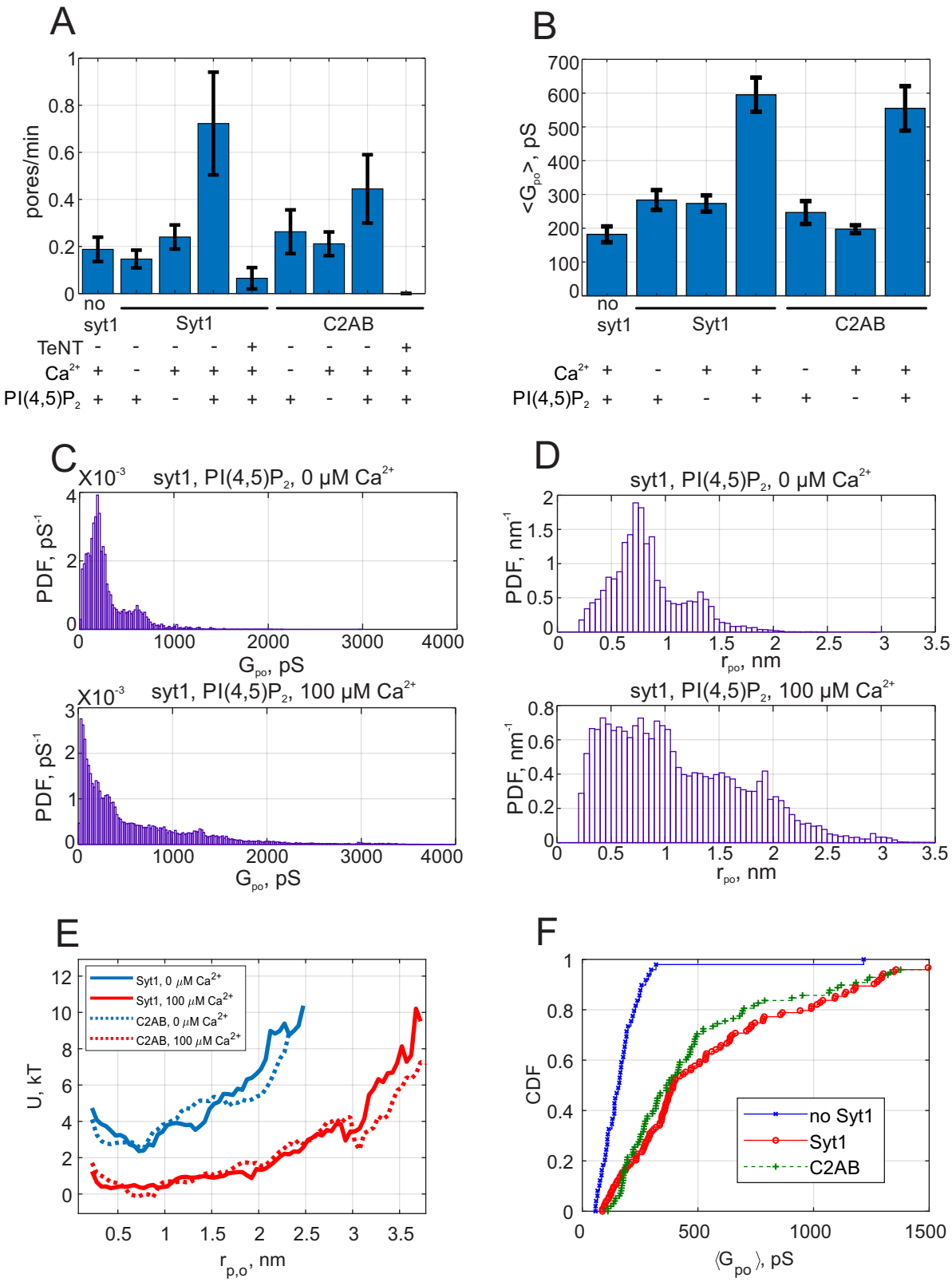

Figure 3

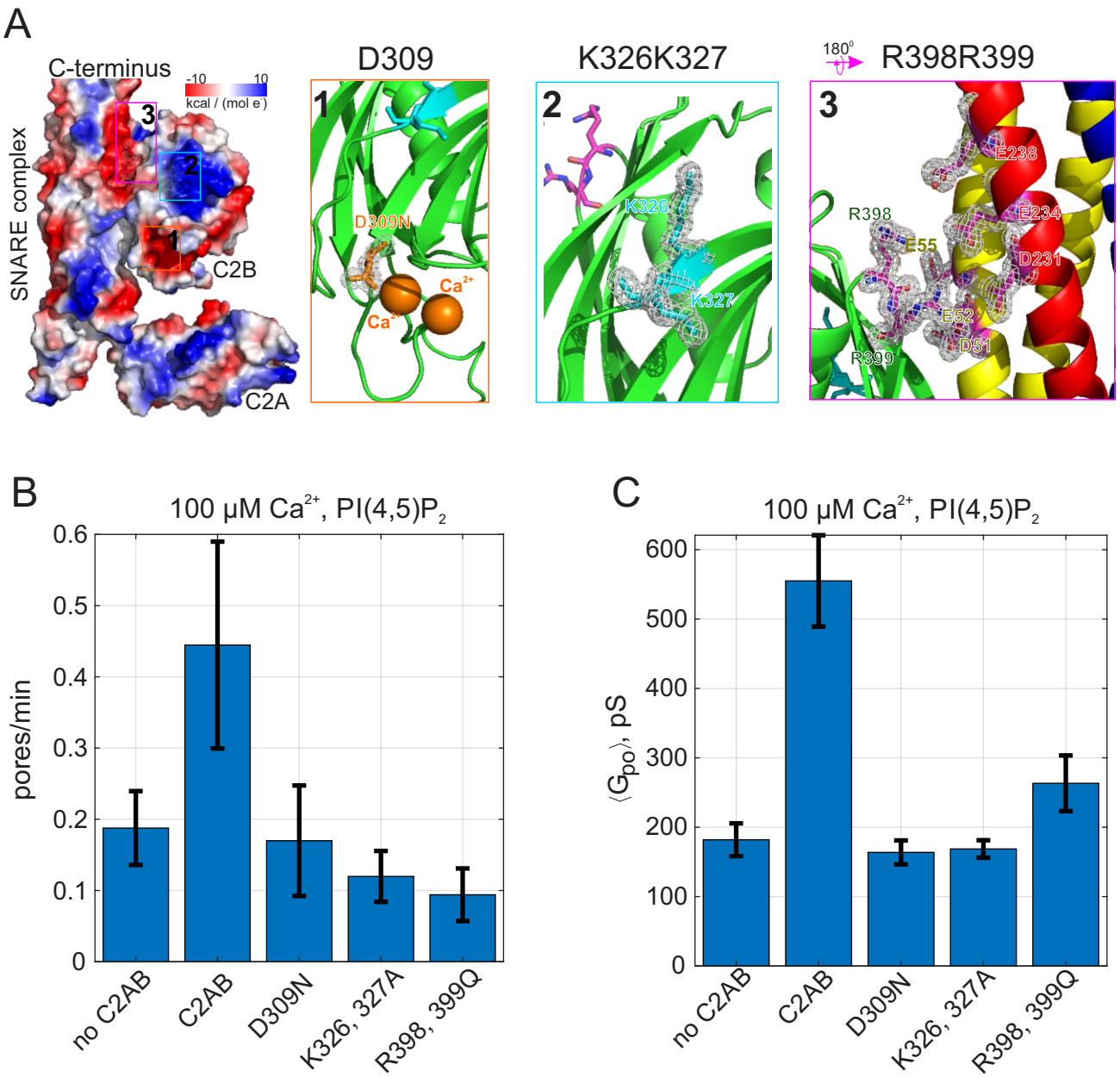

Figure 4

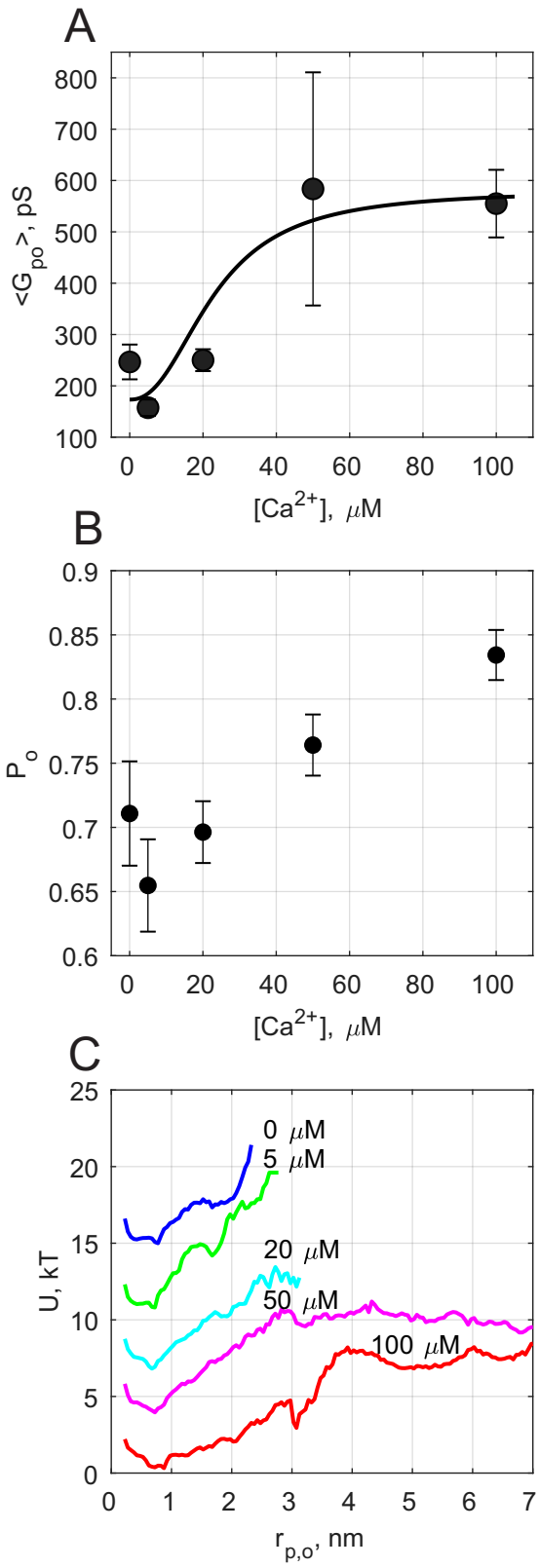

Figure 5

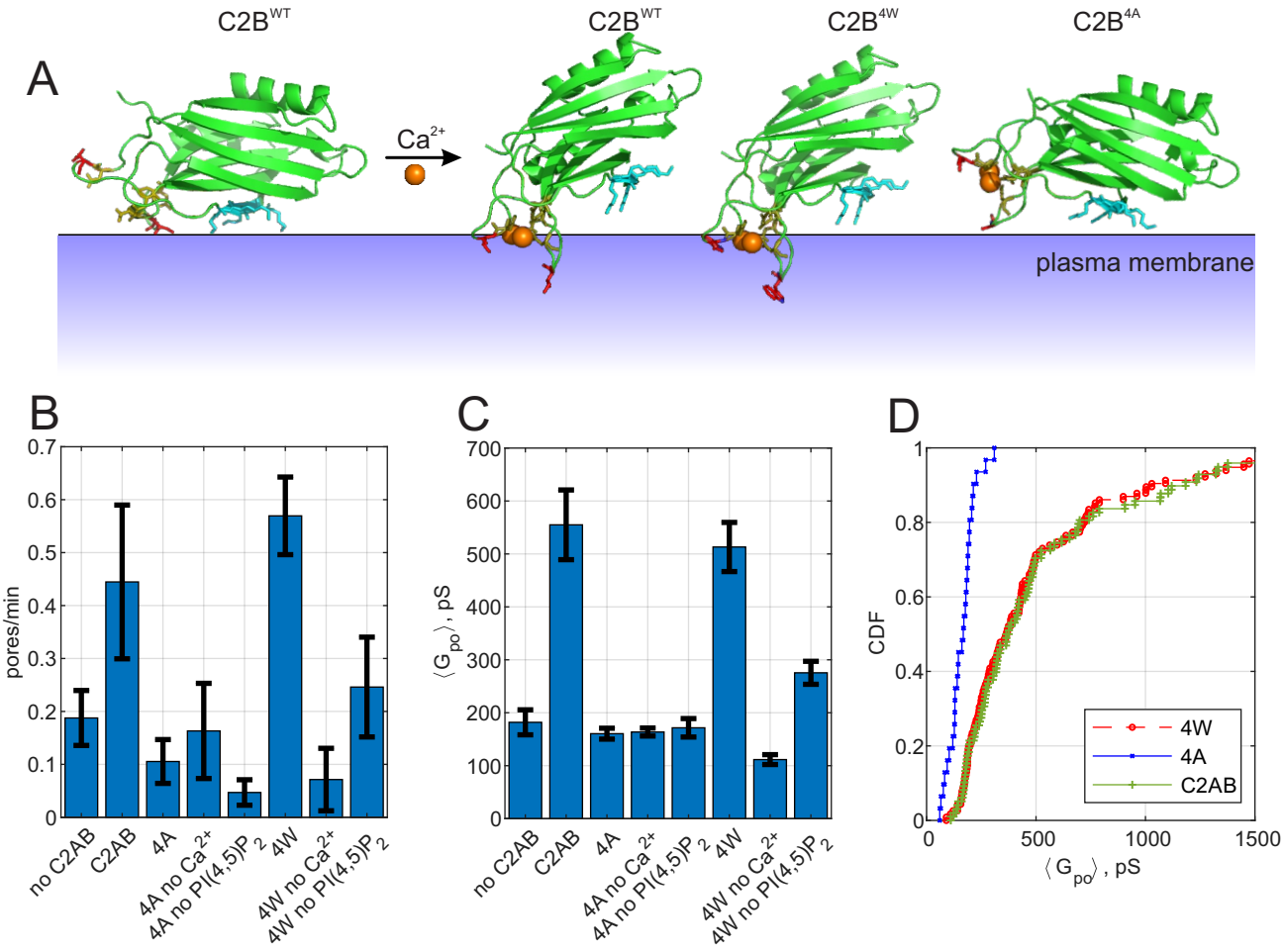

Figure 6

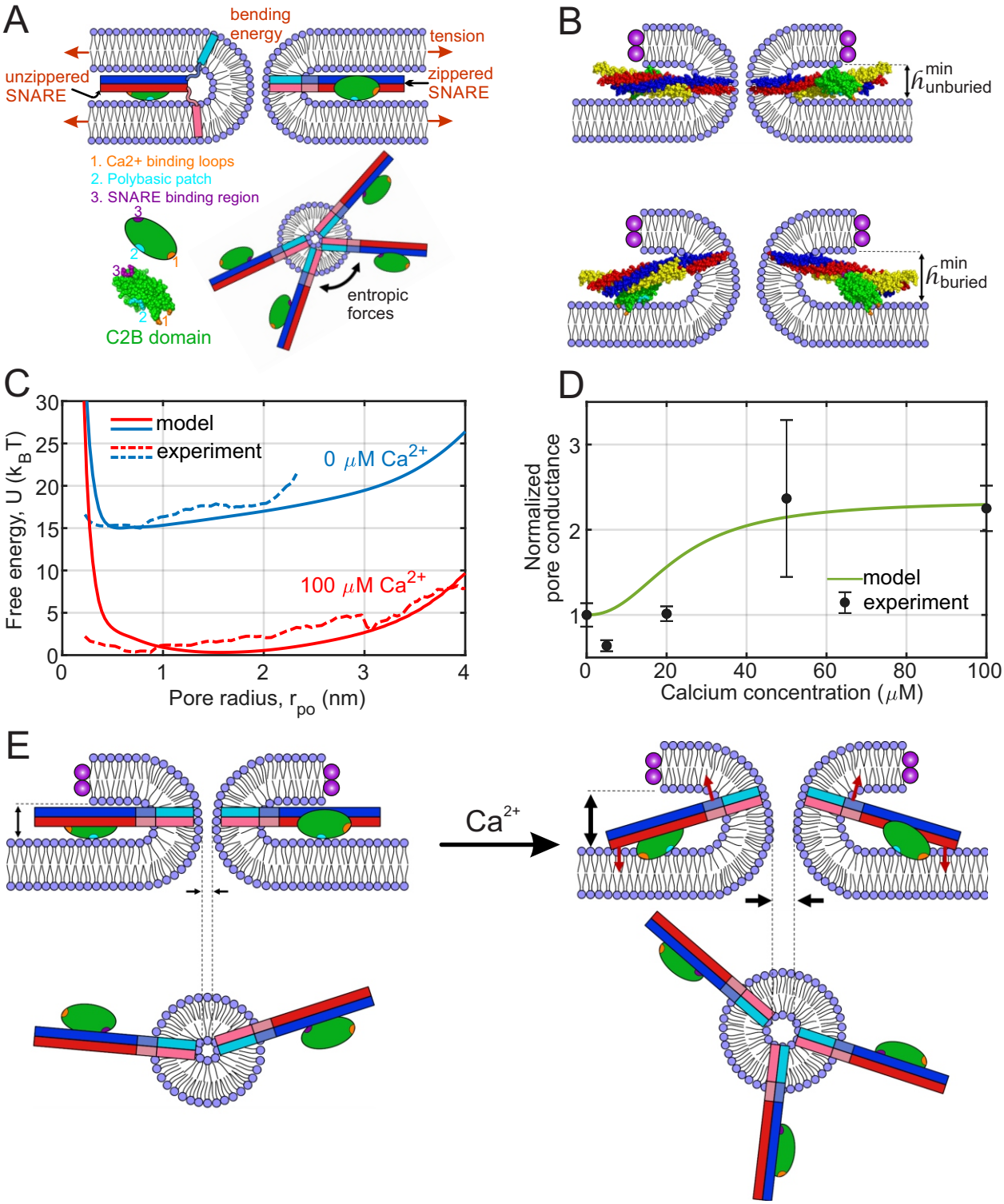

Figure S1

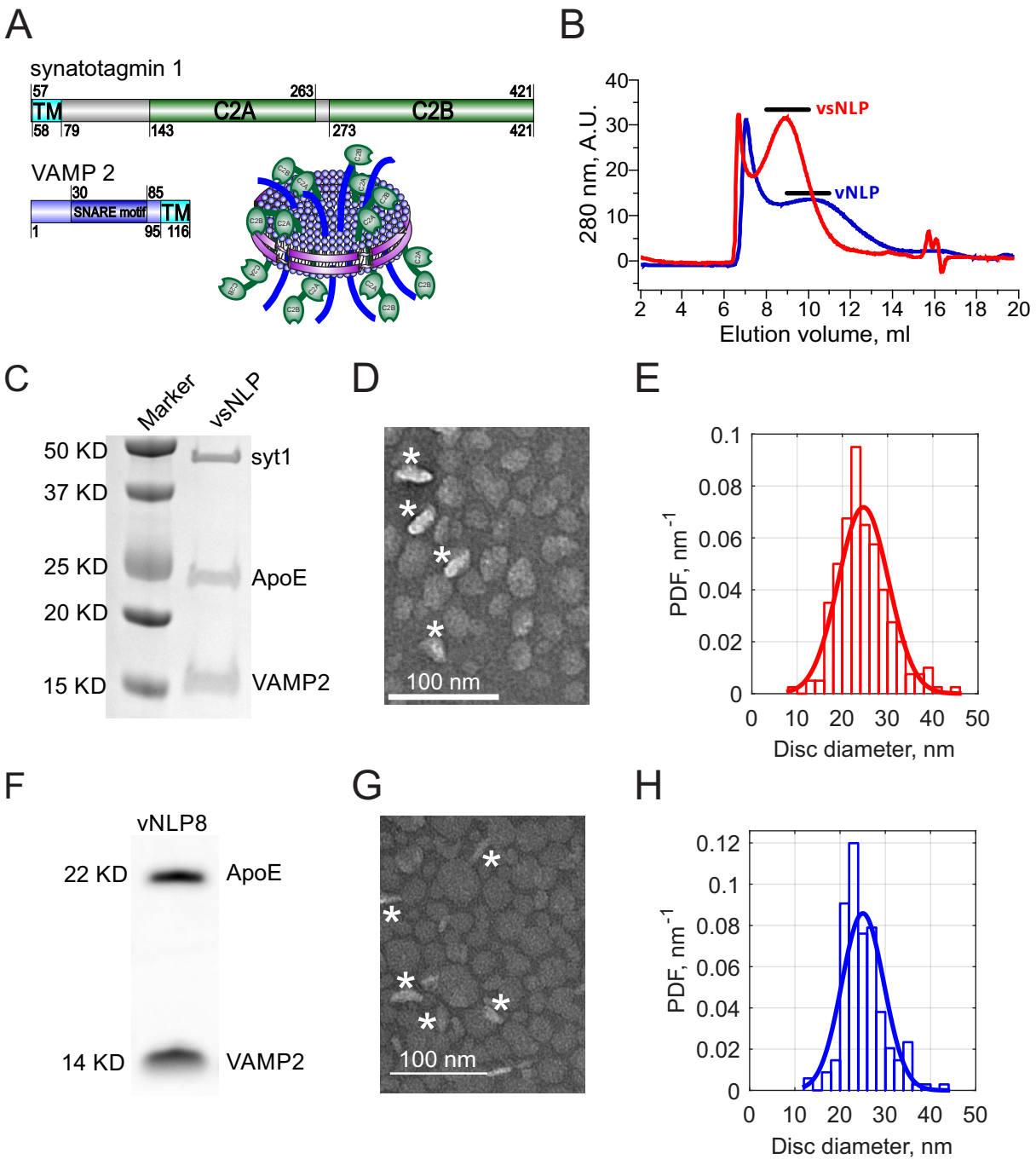

Figure S2

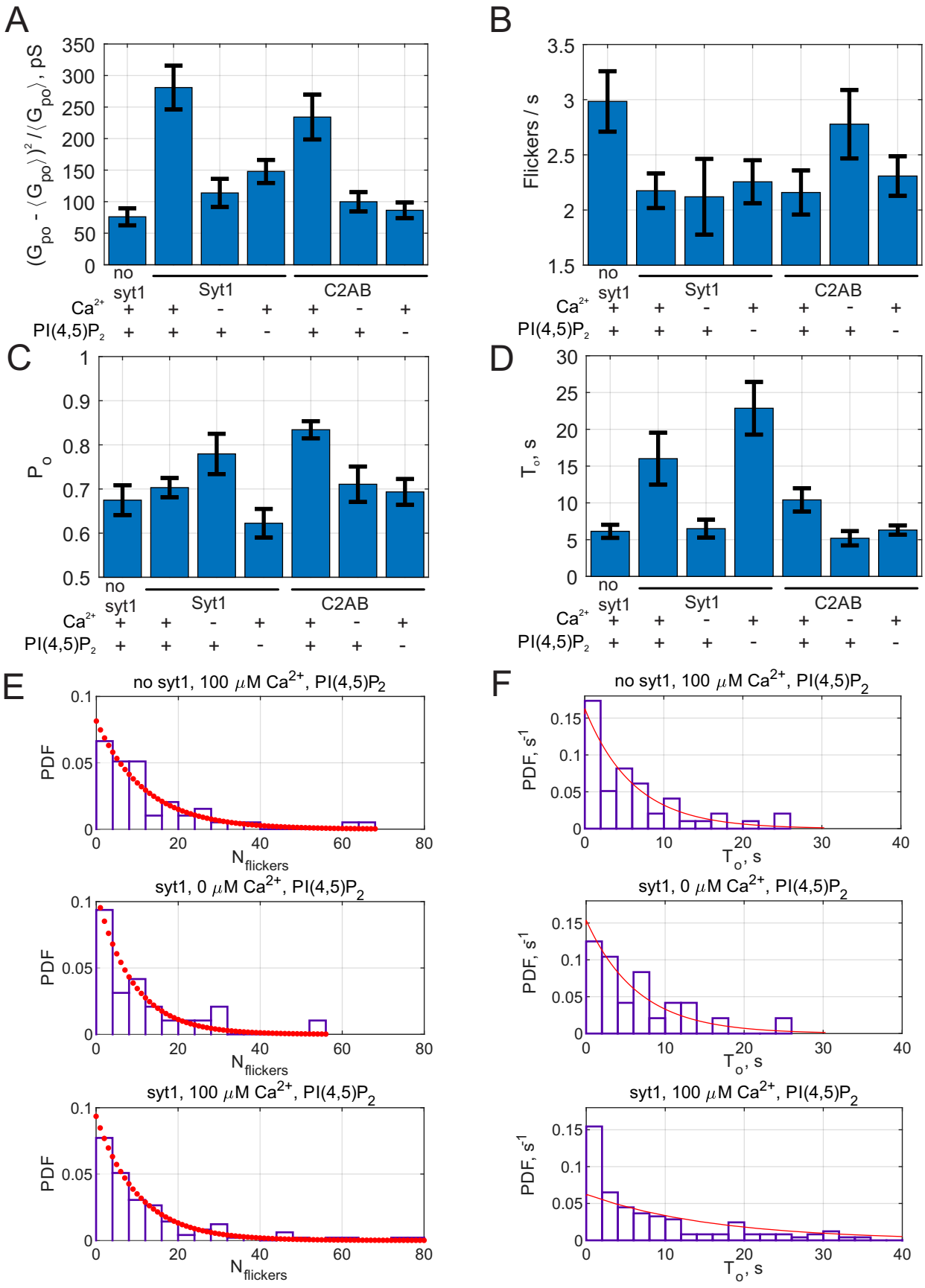

Figure S3

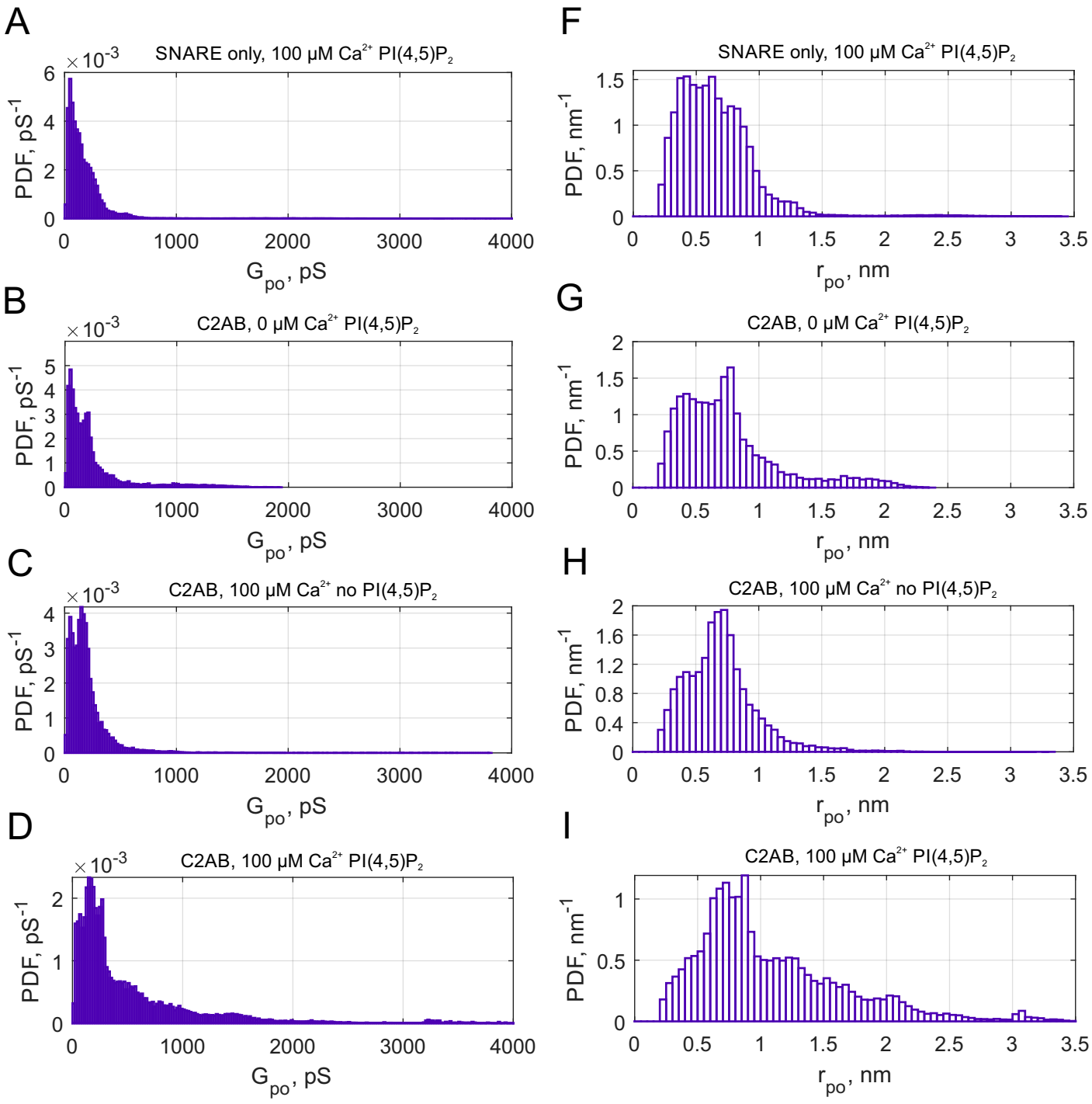

Figure S4

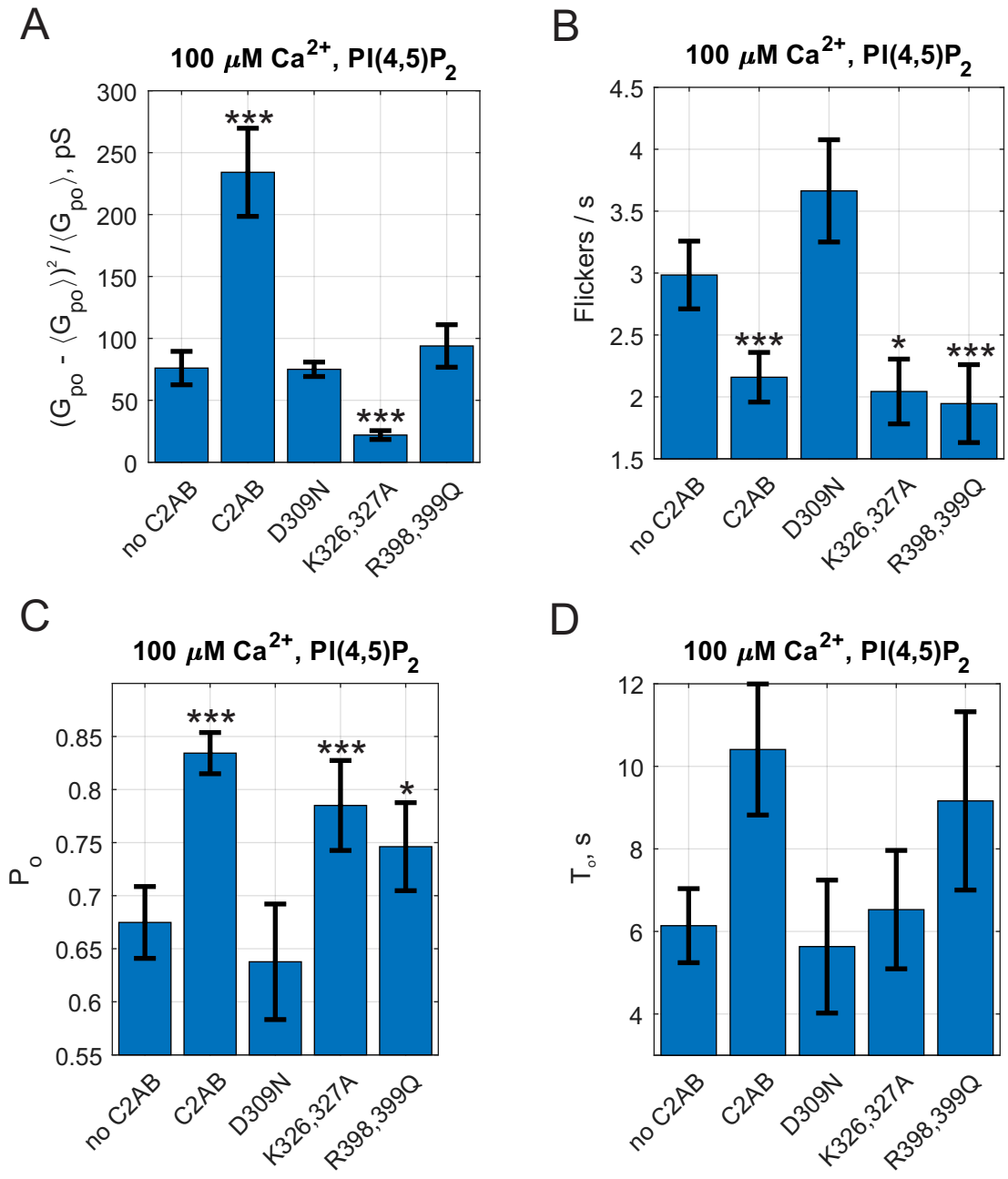

Figure S5

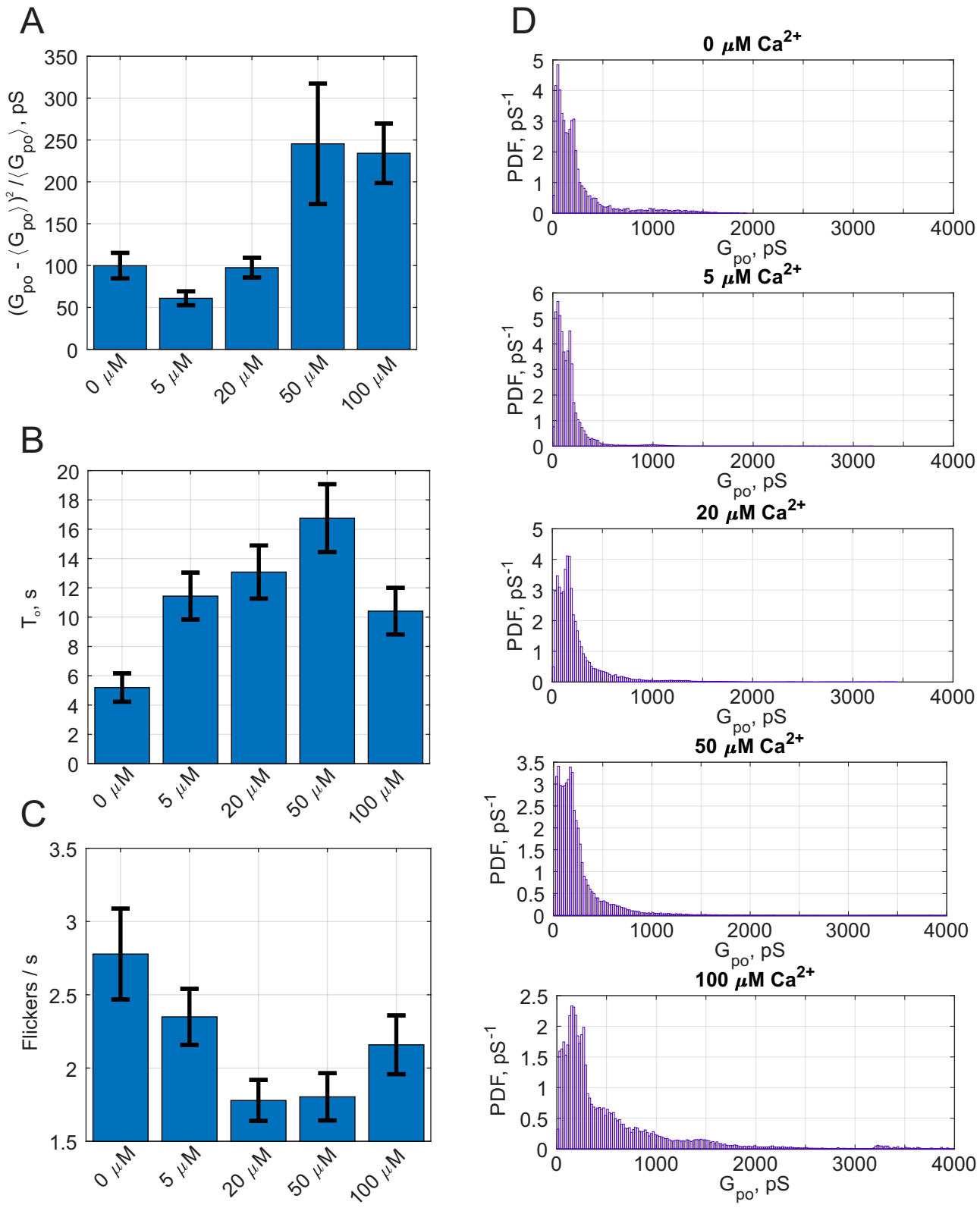

Figure S6

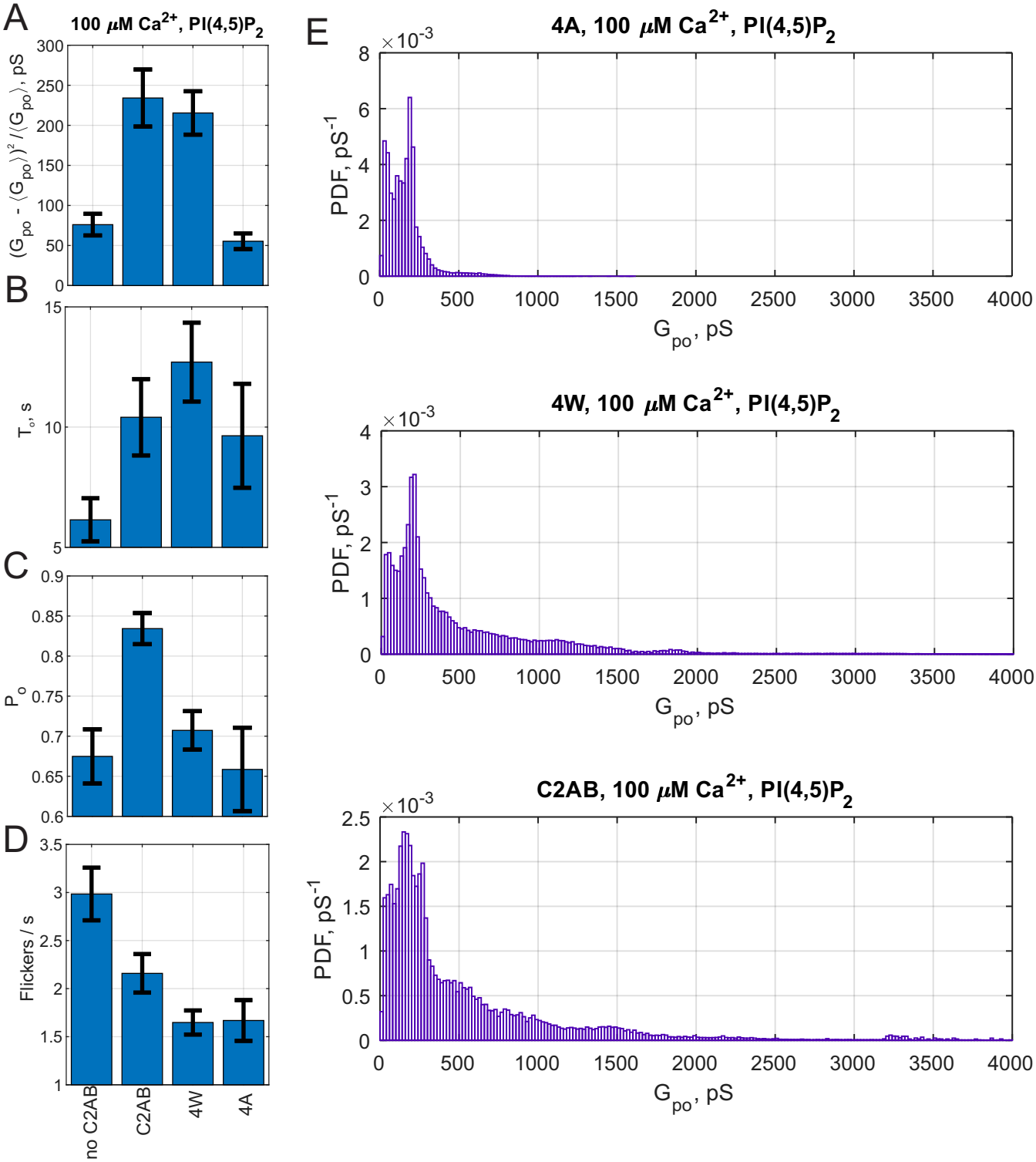

Figure S7